Haverford College
Haverford Scholarship

Faculty Publications | Astronomy

2011

Local Gravity versus Local Velocity: Solutions for β and nonlinear bias

Karen Masters
Haverford College, klmasters@haverford.edu

Marc Davis

Adi Nusser

Follow this and additional works at: https://scholarship.haverford.edu/astronomy_facpubs

Repository Citation

Masters, K.; et al. (2011) "Local Gravity versus Local Velocity: Solutions for β and nonlinear bias." Monthly Notices of the Royal Astronomical Society, 413(4): 2906-2922.

This Journal Article is brought to you for free and open access by the Astronomy at Haverford Scholarship. It has been accepted for inclusion in Faculty Publications by an authorized administrator of Haverford Scholarship. For more information, please contact nmedeiro@haverford.edu.

Monthly Notices
of the
ROYAL ASTRONOMICAL SOCIETY

Mon. Not. R. Astron. Soc. **413,** 2906–2922 (2011) doi:10.1111/j.1365-2966.2011.18362.x

Local gravity versus local velocity: solutions for β and non-linear bias

Marc Davis,[1⋆] Adi Nusser,[2] Karen L. Masters,[3] Christopher Springob,[4] John P. Huchra[5] and Gerard Lemson[6]

[1]*Departments of Astronomy & Physics, University of California, Berkeley, CA 94720, USA*
[2]*Physics Department and the Asher Space Science Institute-Technion, Haifa 32000, Israel*
[3]*Institute for Cosmology and Gravitation, University of Portsmouth, Dennis Sciama Building, Burnaby Road, Portsmouth PO1 3FX*
[4]*Anglo-Australian Observatory, PO Box 296, Epping, NSW 1710, Australia*
[5]*Harvard–Smithsonian Center for Astrophysics, 60 Garden Street, Cambridge, MA 02138, USA*
[6]*Max-Planck Institute of Astrophysics, Karl-Schwarzschild-Str. 1, 85741 Garching, Germany*

Accepted 2011 January 14. Received 2011 January 13; in original form 2010 November 12

ABSTRACT

We perform a reconstruction of the cosmological large-scale flows in the nearby Universe using two complementary observational sets. The first, the SFI++ sample of Tully–Fisher (TF) measurements of galaxies, provides a direct probe of the flows. The second, the whole sky distribution of galaxies in the 2MASS (Two Micron All Sky Survey) redshift survey (2MRS), yields a prediction of the flows given the cosmological density parameter, Ω, and a biasing relation between mass and galaxies. We aim at an unbiased comparison between the peculiar velocity fields extracted from the two data sets and its implication on the cosmological parameters and the biasing relation. We expand the fields in a set of orthonormal basis functions, each representing a plausible realization of a cosmological velocity field smoothed in such a way as to give a nearly constant error on the derived SFI++ velocities. The statistical analysis is done on the coefficients of the modal expansion of the fields by means of the basis functions. Our analysis completely avoids the strong error covariance in the smoothed TF velocities by the use of orthonormal basis functions and employs elaborate mock data sets to extensively calibrate the errors in 2MRS predicted velocities. We relate the 2MRS galaxy distribution to the mass density field by a linear bias factor, b, and include a luminosity-dependent, $\propto L^{\alpha}$, galaxy weighting. We assess the agreement between the fields as a function of α and $\beta = f(\Omega)/b$, where f is the growth factor of linear perturbations. The agreement is excellent with a reasonable χ^2 per degree of freedom. For $\alpha = 0$, we derive $0.28 < \beta < 0.37$ and $0.24 < \beta < 0.43$, respectively, at the 68.3 per cent and 95.4 per cent confidence levels (CLs). For $\beta = 0.33$, we get $\alpha < 0.25$ and $\alpha < 0.5$, respectively, at the 68.3 per cent and 95.4 per cent CLs. We set a constraint on the fluctuation normalization, finding $\sigma_8 = 0.66 \pm 0.10$, which is only 1.5σ deviant from *Wilkinson Microwave Anisotropy Probe* (*WMAP*) results. It is remarkable that σ_8 determined from this local cosmological test is close to the value derived from the cosmic microwave background, an indication of the precision of the standard model.

Key words: cosmological parameters – dark matter – large-scale structure of Universe.

1 INTRODUCTION

For 15 yr, the problem of large-scale flows of galaxies has seen little attention relative to other probes of the large-scale structure in the Universe. The data on peculiar velocities have been difficult to obtain, and the results had contradictory conclusions (Strauss & Willick 1995; Zaroubi 2002). They are limited to small redshifts ($\sim 100\,h^{-1}$ Mpc) at which distance indicators can reliably be used. These earlier forays into the subject led to disagreements that few people wanted to sift through. But in the interval, the data have improved dramatically, thus stirring recent activity in the subject.

Peculiar velocities are unique in that they provide explicit information on the three-dimensional mass distribution, and measure mass on scales of 20–50 h^{-1} Mpc, a scale untouched by alternative methods. Local peculiar velocity data are, in principle,

⋆E-mail: mdavis@berkeley.edu

© 2011 The Authors
Monthly Notices of the Royal Astronomical Society © 2011 RAS

Downloaded from https://academic.oup.com/mnras/article-abstract/413/4/2906/965330
by guest
on 27 February 2018

affluent in cosmological information. Power spectra and correlation functions could be derived from the data by direct calculation or by maximum likelihood techniques (e.g. Gorski et al. 1989; Jaffe & Kaiser 1995; Freudling et al. 1999; Juszkiewicz et al. 2000; Bridle et al. 2001; Abate & Erdoğdu 2009). Direct analysis of low order moments of the flow, such as the bulk motion and the shear, could also be analysed within the framework of cosmological models (e.g. Feldman, Watkins & Hudson 2010). Some authors claim the bulk flow of mixed catalogues of galaxies argues there are problems with Λcold dark matter (CDM) (Watkins, Feldman & Hudson 2009), but recent results (Nusser & Davis 2011) show that the SFI++ catalogue by itself has a large-scale bulk flow that is consistent with ΛCDM, and this analysis has smaller error bars. Other, perhaps more ambitious, applications could involve an assessment of the statistical nature of the initial cosmological large-scale fluctuations, i.e. whether Gaussian or otherwise (Nusser & Dekel 1993; Bernardeau et al. 1995). All these analyses could be performed with peculiar velocity measurements alone.

Here, we will be concerned with a comparison of the observed peculiar velocities on the one hand and the velocities derived from the fluctuations in the galaxy distribution on the other hand. The basic physical principle behind this comparison is simple. The large-scale flows are almost certainly the result of the process of gravitational instability with overdense regions attracting material, and underdense regions repelling material. Initial conditions in the early Universe might have been somewhat chaotic, so that the original peculiar velocity field (i.e. deviations from Hubble flow) was uncorrelated with the mass distribution, or even contained vorticity. But those components of the velocity field which are not coherent with the density fluctuations will adiabatically decay as the Universe expands, and so at late times one expects the velocity field to be aligned with the gravity field, at least in the limit of small amplitude fluctuations (Peebles 1980; Nusser et al. 1991). In the linear regime, this relation implies a simple proportionality between the gravity field $\boldsymbol{g}$ and the velocity field $\boldsymbol{v}_{\rm g}$, namely $\boldsymbol{v}_{\rm g} \propto \boldsymbol{g}t$ where the only possible time t is the Hubble time. The exact expression depends on the mean cosmological density parameter Ω and is given by (Peebles 1980)

$$\boldsymbol{v}_{\rm g}(r) = \frac{2f(\Omega)}{3H_0\Omega}\boldsymbol{g}(\boldsymbol{r}). \tag{1}$$

Given complete knowledge of the mass fluctuation field $\delta_\rho(\boldsymbol{r})$ over all space, the gravity field $\boldsymbol{g}(\boldsymbol{r})$ is

$$\boldsymbol{g}(\boldsymbol{r}) = G\bar{\rho}\int d^3\boldsymbol{r}'\delta_\rho(\boldsymbol{r}')\frac{\boldsymbol{r}'-\boldsymbol{r}}{|\boldsymbol{r}'-\boldsymbol{r}|^3}, \tag{2}$$

where $\bar{\rho}$ is the mean mass density of the Universe. If the galaxy distribution at least approximately traces the mass on large scale, with linear bias b between the galaxy fluctuations $\delta_{\rm G}$ and the mass fluctuations (i.e. $\delta_{\rm g} = b\delta_\rho$), then from (1) and (2) we have

$$\boldsymbol{v}_{\rm g}(r) = \frac{H_0\beta}{4\pi\bar{n}}\sum_i \frac{1}{\phi(r_i)}\frac{\boldsymbol{r}_{\rm i}-r}{|r_{\rm i}-r|^3} + \frac{H_0\beta}{3}\boldsymbol{r}, \tag{3}$$

where $\bar{n}$ is the true mean galaxy density in the sample, $\beta \equiv f(\Omega)/b$ with $f \approx \Omega^{0.55}$ the linear growth factor (Linder 2005), and where we have replaced the integral over space with a sum over the galaxies in a catalogue, with radial selection function $\phi(r)$.[1] The second term is for the uniform component of the galaxy distribution and would exactly cancel the first term in the absence of clustering within the survey volume. Note that the result is insensitive to the value of H_0, as the right-hand side has units of velocity. We shall henceforth quote all distances in units of km s^{-1}. The sum in equation (3) is to be computed in real space, whereas the galaxy catalogue exists in redshift space. As we shall see in Section 3.1, the modified equation, which includes redshift distortions, maintains a dependence on Ω and b through the parameter β. Therefore, a comparison of the measured velocities of galaxies to the predicted velocities, $\boldsymbol{v}_{\rm g}(r)$, gives us measure of β. Further, a detailed comparison of the flow patterns addresses fundamental questions regarding the way galaxies trace mass on large scales and the validity of gravitational instability theory.

In this paper we shall make this comparison using the best presently available data for both the velocity and gravity fields. The direct comparison of the peculiar velocities is fraught with difficulty. Distances to individual galaxies are typically uncertain at the 20 per cent level and are furthermore subject to considerable Malmquist bias. We shall elaborate a method that was first presented 15 yr ago (Davis, Nusser & Willick 1996, hereafter DNW96) and which was designed to alleviate most of the observational biases. But the peculiar velocity data at that time were poor and our results as well as those of others (e.g. Yahil 1988; Strauss & Davis 1988; Kaiser et al. 1991; Branchini et al. 2001a; Hudson et al. 1995; Nusser et al. 2001; Zaroubi et al. 2002) were all meant to be preliminary and none of their conclusions was compelling.

Recently, ideal data sets have been assembled, thus allowing a new, definitive analysis of large-scale flows. The new gravity field is very well described by the nearly whole sky Two Mass Redshift Survey (2MRS) (Huchra et al. 2005), and the new peculiar velocity catalogue is the SFI++ sample (Springob et al. 2007, 2009). The 2MRS has previously been used to address the gravity field in considerable detail (e.g. Erdoğdu et al. 2006a; Feldman, Hudson & Watkins 2008), and some effort has gone into the comparison of the 2MRS-predicted velocities versus the SFI++ measured velocities, in particular by Pike & Hudson (2005) and Lavaux et al. (2010). To date nobody has included a proper treatment of the correlated noise in the analysis. Here, we shall compare the observed versus predicted radial velocities, taking into account a full error analysis based on a suite of elaborate mock catalogues designed to match the 2MRS and SFI++ data sets. We shall use a refinement of the method of orthogonal mode expansion by Nusser & Davis (1994, hereafter ND94) and (Nusser & Davis 1995, hereafter ND95). As analysis of peculiar velocity data is inevitably plagued by systematics, random measurement errors and sparseness of the data. The methods employed here are specifically designed to minimize these biasing, thus achieving a robust unbiased comparison between the measured SFI++ and the predicted 2MRS velocities.

In Section 2, we introduce the 2MRS and the SFI++ data sets and various trims that we do to ensure unambiguous reliable results. In Section 3 we describe the method for extracting large-scale peculiar motions from both data sets. We discuss the linear equation for predicting the peculiar velocity field associated with a distribution of galaxies in redshift space and review our old method deriving estimates of galaxy peculiar velocities from the inverse Tully–Fisher (ITF) relation by means of an expansion over orthonormal modes (basis functions). We focus on the new refinements designed to optimize the extraction of the signal from the data. As has been the case in the past, mock catalogues constructed from N-body simulations are essential for debugging and calibrating the methods. This is especially so for our application, since the entire analysis is performed in essentially pure redshift space. We present details of the mocks in Section 4. In Section 5 we inspect the flow fields reconstructed from

[1] $\phi(r)$ is defined as the fraction of the luminosity distribution function observable at distance r for a given flux limit; see (e.g. Yahil et al. 1991).

Downloaded from https://academic.oup.com/mnras/article-abstract/413/4/2906/965330
by guest
on 27 February 2018

the 2MRS and SF++ data, visually and statistically, demonstrating that differences between them are similar to those expected in the mocks. We present our constraints on the cosmological parameters in Section 6. In the concluding Section 7 we summarize our findings, discussing their implications and contrasting them with other results in the literature. For readers wanting to avoid the 'how to' details, we suggest skipping Sections 3 and 4 but then coming back to understand how our machinery operates.

2 NEW DATA FOR THE COMPARISON

2.1 Gravity field

20 yr ago the only catalogue of galaxy photometry with uniform coverage over the full sky was derived from the *IRAS* satellite (Strauss & Davis 1988; Yahil 1988). From the point source catalogue (galaxies were unresolved in *IRAS*) a flux-limited sample at 60 μm was constructed and redshifts were obtained for all objects to construct the *IRAS* Point Source Catalogue redshift survey (PSCz; Fisher et al. 1995a). Among other problems, this PSCz catalogue gave little weight to ellipticals (which are dim at 60 μm as this wavelength is dominated by dusty star formation) and suffered from severe confusion in regions of high density. However, the uniform full-sky coverage was unique in enabling the estimation of local gravity, and furthermore our local gravity field (in a relatively low density region of the Universe) is dominated by spiral, not elliptical, galaxies and *IRAS* gave a fair, although noisy, representation of the spirals.

Much larger redshift surveys do now exist, e.g. Sloan Digital Sky Survey (SDSS; Abazajian et al. 2009) and 2dF (Colless et al. 2003), but few have attempted to be complete over the whole sky as many cosmological measurements do not require such complete surveys and a trade off has been made between depth and sky coverage from the available telescope time and resources. The most recent *all sky* imaging survey was the Two Micron All-Sky Survey (2MASS; Skrutskie et al. 2006), and the 2MASS Extended Source Catalogue (XSC; Jarrett et al. 2000) extracts from that imaging a flux-limited (to $K = 13.5$) sample of half a million extragalactic objects. The 2MRS (Huchra et al. 2005) is a program to obtain redshifts for all galaxies in the 2MASS XSC to a fixed flux limit in the K band. The $K = 11.25$ mag limited version of 2MRS consists of 23 000 galaxy redshifts with uniform sky coverage to within 5° of the Galactic plane except towards the Galactic centre where stellar confusion limits the catalogue to ±10° (Huchra et al. 2005b). A$K =$ 11.75 mag limited version of 2MRS is almost complete, consists of 43 000 galaxy redshifts and will be made available soon (Huchra et al. in preparation). Since the sample is K-band selected, the extinction correction is modest and it is ideal for calculating local gravity.

In the Southern hemisphere redshifts for the 2MASS galaxies were observed as part of the 6dFGS (Jones et al. 2005, 2009), which used the 6dF multi-fibre spectrograph on the 1.2-m UK Schmidt in Siding Spring, Australia. Their ultimate product was a map of 110 256 2MASS galaxies in the southern sky to a magnitude limit of $K = 12.75$ mag and to within 10° of the Galactic plane. This survey is far deeper than the stated goal of 2MRS, but also has a higher Galactic latitude limit. In the Northern hemisphere, the 2MRS builds on a strong tradition of redshift surveys at the CfA: the CfA redshift survey and ZCAT (Davis et al. 1982; de Lapparent, Geller & Huchra 1986). In the absence of a Northern hemisphere equivalent to the 6dF, new redshift observations are done galaxy by galaxy using the 1.2-m telescope at the Fred Lawrence Whipple Observatory on Mt. Hopkins, AZ. The average density of galaxies at the magnitudes 2MRS is observing is about 1 per degree, so without a wide-field multi-object spectrograph in the Northern hemisphere this remains the most efficient way to get new redshifts. Lower Galactic latitude galaxies in the Southern hemisphere ($|b| > 5$) were added to 2MRS from observations at CTIO. The version of the 2MRS which is complete to $K = 11.25$ (consisting of 23 200 galaxies; Huchra et al. 2005; Westover 2007) has been used to calculate the acceleration on the Local Group (LG) by Erdoğdu et al. (2006b). The dipole estimate seems to converge to the cosmic microwave background (CMB) result within $60\,h^{-1}$ Mpc, suggesting that the bulk of the motion of the LG comes from structures within that distance. They also have done a dipole analysis, weighting the sample by its luminosity, rather than the counts, and find relatively minor changes. Density and velocity fields have been calculated by Erdoğdu et al. (2006a) for the $K = 11.25$ sample. All major local superclusters and voids are successfully identified, and backside infall on to the 'Great Attractor' region (at $50\,h^{-1}$ Mpc) is detected.

The 2MRS catalogue appears to be a fair tracer of the underlying mass distribution. The real–space correlation lengths, r_0, is best fit by a regression $r_0 = (7.5 \pm 0.5) - (3.0 \pm 0.6)\log_{10}n$, where n is the cumulative number density in $10^{-3}\,h^3$ Mpc (Westover 2007). In contrast, Zehavi et al. (2010) report that the R band optically selected SDSS survey gives $r_0 = (6.7 \pm 0.1) - (2.0 \pm 0.1)\log_{10}n$. In terms of bias estimates, Westover (2007) reports $b/b_* = 0.73 + 0.24L/L_*$ while Norberg et al. (2002) state that $b/b_* = 0.85 + 0.15L/L_*$ for the 2DF survey. In other words, Westover's data show the 2MRS correlations are more dependent on luminosity than are optically selected samples. In view of this luminosity-dependent result, it makes the most sense to evaluate the gravity field in a luminosity-weighted manner; it is computed below with a variety of luminosity weightings. Westover (2007) has also made a mock catalogue for the missing galaxies at low latitude by interpolating the galaxy density above and below them in three dimensions. We shall use this catalogue as an estimate of the local mass density.

2.2 TF sample

20 yr ago, the mis-calibration of full sky Tully–Fisher (TF) data was the problem that led to very discrepant results for the determination of $\beta \equiv \Omega/b$, with $\beta = 0.5 \pm 0.2$ (DNW96) and $\beta = 1.0 \pm 0.2$ (e.g. Dekel et al. 1993). The mistaken TF calibration led to a large-scale flow that confused both analyses, but in the end, it was a calibration error in the southern sky which made a false large-scale flow (Willick et al. 1997). In one analysis, this led to a higher χ^2 than was acceptable, and in the other it led to a biased result.

For the analysis given below, we use the recently completed survey of spiral galaxies with I-band TF distances, SFI++ (Masters et al. 2006; Springob et al. 2007, 2009), which in turn builds on the original Spiral Field I-band Survey (Giovanelli et al. 1994, 1995; Haynes et al. 1999) and Spiral Cluster I-band Survey (Giovanelli et al. 1997a,b). We use the published SFI++ magnitudes and velocity widths, and derive our own peculiar velocities, rather than taking the published distances as given. We use the SFI++ catalogue as it includes several data sets to give full sky coverage. It is not essential for our analysis that the peculiar velocity sample have uniform sky coverage, but they must have a uniform calibration.

The other major TF catalogue was published by Tully et al. (2008). This survey is restricted to $cz < 3000\,\mathrm{km\,s^{-1}}$, and includes many of the same galaxies in that redshift range as SFI++. Tully also make use of a different algorithm for measuring spectral linewidths, which are not easily comparable to the values derived for SFI++. So while one could in principle combine the two

Downloaded from https://academic.oup.com/mnras/article-abstract/413/4/2906/965330
by guest
on 27 February 2018

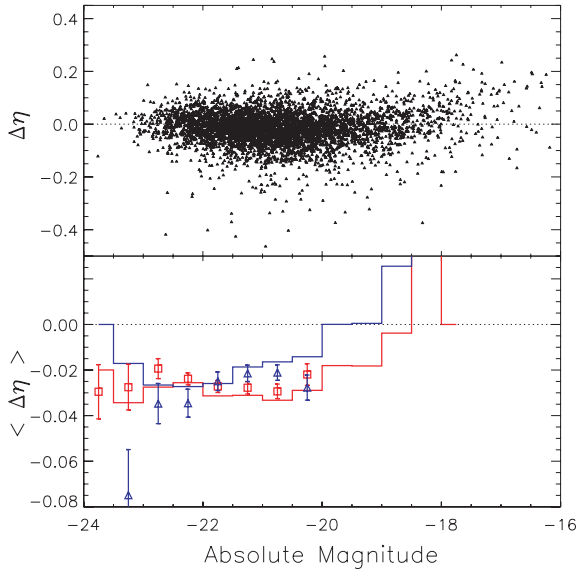

Figure 1. Top: the scatter of the η–M_I relationship, where $\gamma = 0.12$. Bottom: the mean $\Delta\eta$ in 0.5 mag bins of the raw distribution [recall that $\eta = \log(W)$]. The red is for galaxies with $cz > 5000\,\mathrm{km\,s^{-1}}$, while the blue is for $cz < 5000\,\mathrm{km\,s^{-1}}$. Note the change where $M_I > -20$, and also how the red and blue curves appear to have different TF relations. The histograms are for the raw data, with no flow model, while the points, with 1σ error bars, are the mean values of $\eta - M_I$ after the fit. The nearby and more distant galaxies now have identical TF relations.

catalogues for this analysis, the small potential gain in sample size is not enough to justify the resulting heterogeneity in observational methods and data analysis.

We shall use the inferred distances, as well as redshifts, to derive an estimate of peculiar velocity for each galaxy. Correlation analysis (Borgani et al. 2000) indicates that peculiar velocities in the SFI++ behave as expected for ΛCDM models (see especially Branchini et al. 2001b; Freudling et al. 1999; da Costa et al. 1998; Feldman & Watkins 2008).

In the analysis given below, we shall use the ITF relationship, as given in equation (8). We begin by drawing the published magnitudes, velocity widths and redshifts from Springob et al. (2007, 2009). We include all field, group and cluster galaxies, which leaves us with an initial sample of 4859 galaxies. Galaxies in groups and clusters are treated as individual objects, though the redshifts for template cluster galaxies are replaced by the systematic redshift of the cluster. Following Giovanelli et al. (1997a), we brighten the magnitudes of Sb galaxies by 0.10 mag and brighten the magnitudes of spirals earlier than Sb by 0.32 mag, while leaving types later than Sb unchanged. This is done in order to account for subtle differences in the TF relation of different spiral subclasses. We select only objects with inclination $i > 45^\circ$ to ease problems with inclination corrections. The data must be transformed to the LG frame, and galaxies with $cz < 200\,\mathrm{km\,s^{-1}}$ are deleted. All the analysis is done in the LG frame as the boundary conditions then simply become $v_\mathrm{g} \to 0$ and $v_\mathrm{ITF} \to 0$.

The few galaxies with large residual $\Delta\eta$ ($\Delta\eta$ is the residual from equation 8; see Fig. 1) are sufficiently deviant to be a worry for statistics which depend on data with a compact core and no long tails. The typical outlying object is not unusually nearby in redshift, and peculiar motions cannot be the explanation. The vast majority of SFI++ galaxies have well-behaved TF relationships; perhaps the outliers are undergoing a merger? There are large negative $\Delta\eta$ outliers, but few corresponding large positive $\Delta\eta$ outliers, and this is resolved by clipping the outliers at $|\Delta\eta| > 0.20$.

The top panel of Fig. 1 shows the distribution of $\Delta\eta$ *before* galaxies have had their magnitude changed because of peculiar velocities; in the bottom panel is shown the result of averaging the data into .5 mag bins, where the red histogram is for galaxies at $cz > 5000\,\mathrm{km\,s^{-1}}$ and the blue histogram is for those with $cz < 5000\,\mathrm{km\,s^{-1}}$, in the raw data. The red and blue points, plus $1-\sigma$ error bars, are the average $\langle\Delta\eta\rangle$ versus M *after* the best flow model, described in Section 3.5, is fit to the data. The blue point with $M < -23$ is deviant, but it only represents 11 galaxies, compared to an average of 170 galaxies in the other bins. Note that the zero-point of the $\langle\Delta\eta\rangle$ behaviour makes no difference; only the slope, the constancy of $\langle\Delta\eta\rangle$ versus M is important. Compared to the different slopes before the flow corrections are applied, the TF relation is now identical in the foreground versus the background of the SFI++ data. This figure is for illustration only, as the data are not binned during the fitting process.

The bend in the TF relationship at $M = -20$ is known to be a result of the reduced mass in the Baryonic TF relation (Stark, McGaugh & Swaters 2009; Gurovich et al. 2010). We are missing the data to straighten out the curve, and since the ITF method is easiest to apply if there is a linear relationship between η and M, we simply delete all galaxies with $M > -20$ from further consideration. After all these cuts, we are left with 2830 spiral galaxies with $200 < cz_\mathrm{LG} < 10\,000\,\mathrm{km\,s^{-1}}$.

The raw distribution of $\Delta\eta$, after limiting the sample and fitting the best linear curve, is found to approximately fit a Gaussian with $\sigma = 0.059$. This is the dispersion with *no flow model* applied. The Gaussian width to the distribution is $\sigma = 0.0558$ after the flow model is applied. The small decrease is limited by the intrinsic, dominant noise of the TF relation. This noise has numerous causes, such as the uncertainty in the inclination correction of the SFI++ galaxies, or small variations in the outer limits of the rotation curves of the galaxies.

The following sections, Sections 3 and 5, explain the machinery for effecting this reduction.

3 RECONSTRUCTION OF PECULIAR VELOCITIES

In this section we outline our method described in ND94, ND95 and DNW96 for deriving the smooth peculiar velocities of galaxies from an observed distribution of galaxies in redshift space and, independently, from a sample of spiral galaxies with measured circular velocities η and apparent magnitudes m.

3.1 Peculiar velocities from the distribution of galaxies in redshift space

There are several methods for generating peculiar velocities from redshift surveys, using linear (e.g. Fisher et al. 1995b) and non-linear relations (e.g. Peebles 1980; Croft & Gaztanaga 1998; Nusser & Branchini 2000; Frisch et al. 2002a; Enßlin, Frommert & Kitaura 2009). Here, we restrict ourselves to large scales where linear theory is applicable. We will use the method of ND94 for reconstructing velocities from the 2MRS. This method is particularly convenient, as it is easy to implement, fast and requires no iterations. Most importantly, this redshift-space analysis closely parallels the ITF estimate described below. We next present a very brief summary of the methodology.

Downloaded from https://academic.oup.com/mnras/article-abstract/413/4/2906/965330
by guest
on 27 February 2018

We follow the notation of DNW96. The comoving redshift-space coordinate and the comoving peculiar velocity relative to the LG are, respectively, denoted by $\boldsymbol{s}$ (i.e. $s = cz/H_0$) and $\boldsymbol{v}(\boldsymbol{s})$. To the first order, the peculiar velocity is irrotational in redshift space (Chodorowski & Nusser 1999) and can be expressed as $\boldsymbol{v}_{\rm g}(\boldsymbol{s}) = -\nabla\Phi(\boldsymbol{s})$ where $\Phi(\boldsymbol{s})$ is a potential function. As an estimate of the fluctuations in the fractional density field $\delta_0(\boldsymbol{s})$ traced by the discrete distribution of galaxies in redshift space we consider

$$\delta_0(\boldsymbol{s}) = \frac{1}{(2\pi)^{3/2}\bar{n}\sigma^3}\sum_i \frac{w(L_{0i})}{\phi(s_i)}\exp\left[-\frac{(\boldsymbol{s}-\boldsymbol{s}_i)^2}{2\sigma^2}\right] - 1, \tag{4}$$

where $\bar{n} = \sum_i w(L_{0i})/\phi(s_i)$ and w weighs each galaxy according to its estimated luminosity, L_{0i}. The 2MRS density field is here smoothed by a Gaussian window with a redshift-independent width, $\sigma = 350\,{\rm km\,s^{-1}}$. This is in contrast to DNW96 where the *IRAS* density was smoothed with a width proportional to the mean particle separation. The reason for adopting a constant smoothing for 2MRS is its dense sampling which is nearly four time higher than *IRAS*. We emphasize that the coordinates $\boldsymbol{s}$ are in *observed redshift* space, expanded in a galactic reference frame. The only corrections from pure redshift-space coordinates is the collapse of the fingers of god of the known rich clusters prior to the redshift-space smoothing (Yahil et al. 1991). Weighting the galaxies in equation (4) by the selection function and luminosities evaluated at their redshifts rather than the actual (unknown) distances yields a biased estimate for the density field. This bias gives rise to Kaiser's rocket effect (Kaiser 1987).

To construct the density field, equation (4), we volume limit the 2MRS sample to $3000\,{\rm km\,s^{-1}}$, so that $\phi(s < 3000) = 1$, resulting in $\phi(s = 10\,000) = 0.27$ (Westover 2007). In practice, this means we delete galaxies from the 2MRS sample fainter than $M_* + 2$. Galaxies at $10\,000\,{\rm km\,s^{-1}}$ therefore have $1/\phi = 3.7$ times the weight of foreground galaxies in the generation of the velocity field, $v_{\rm g}$.

If we expand the angular dependence of Φ and $\delta_0(\boldsymbol{s})$ redshift space in spherical harmonics in the form

$$\Phi(\boldsymbol{s}) = \sum_{l=0}^{\infty}\sum_{m=-l}^{l}\Phi_{lm}(s)Y_{lm}(\theta,\varphi) \tag{5}$$

and similarly for δ_0, then, to the first order, Φ_{lm} and δ_{0lm} satisfy

$$\frac{1}{s^2}\frac{\rm d}{{\rm d}s}\left(s^2\frac{{\rm d}\Phi_{lm}}{{\rm d}s}\right) - \frac{1}{1+\beta}\frac{l(l+1)\Phi_{lm}}{s^2} = \frac{\beta}{1+\beta}\left(\delta_{0lm} - \kappa(s)\frac{{\rm d}\Phi_{lm}}{{\rm d}s}\right), \tag{6}$$

where

$$\kappa = \frac{{\rm d}\ln\phi}{{\rm d}s} - \frac{2}{s}\frac{d\ln w(L_{0i})}{d\ln L_{0i}} \tag{7}$$

represents the correction for the bias introduced by the generalized Kaiser rocket effect. As emphasized by ND94, the solutions to equation (6) for the monopole ($l = 0$) and the dipole ($l = 1$) components of the radial peculiar velocity in the LG frame are uniquely determined by specifying vanishing velocity at the origin. That is, the radial velocity field at redshift $\boldsymbol{s}$, when expanded to harmonic $l \leq 1$, is not influenced by material at redshifts greater than $\boldsymbol{s}$.

In this paper, we shall consider solutions as a function of β and the parameter α defining a power-law form $w_i \propto L_i^{\alpha}$ for the galaxy weights.

3.2 Peculiar velocities from the inverse Tully–Fisher relation

Given a sample of galaxies with measured circular velocity parameters, $\eta_i \equiv \log\omega_i$, linewidth ω_i, apparent magnitudes m_i and redshifts z_i, the goal is to derive an estimate for the smooth underlying peculiar velocity field. We assume that the circular velocity parameter, η, of a galaxy is, up to a random scatter, related to its absolute magnitude, M, by means of a linear ITF relation, i.e.

$$\eta = \gamma M + \eta_0. \tag{8}$$

One of the main advantages of inverse TF methods is that samples selected by magnitude, as most are, will be minimally plagued by Malmquist bias effects when analysed in the inverse direction (Schechter 1980; Aaronson et al. 1982). We write the absolute magnitude of a galaxy,

$$M_i = M_{0i} + P_i \tag{9}$$

where

$$M_{0i} = m_i + 5\log(z_i) - 15 \tag{10}$$

and

$$P_i = 5\log(1 - u_i/z_i), \tag{11}$$

where m_i is the apparent magnitude of the galaxy, z_i is its redshift in units of ${\rm km\,s^{-1}}$ and u_i is its radial peculiar velocity in the LG frame.

ND95 base a velocity model on spherical harmonics and spherical Bessel functions, for galaxies distributed over the sky to $6000\,{\rm km\,s^{-1}}$. With the 2MRS we extend the gravity field to $10\,000\,{\rm km\,s^{-1}}$. In general, one can write the function P_i in terms of an expansion over $j_{\rm m}$ orthogonal basis functions, F_i^j,

$$P_i = \sum_{j=0}^{j_{\rm m}} a^j F_i^j \tag{12}$$

with orthonormality conditions,

$$\sum_{i=1}^{N_{\rm g}} F_i^j F_i^{j'} = \delta_K^{j,j'}, \tag{13}$$

and the zeroth mode defined by $F_i^0 = 1/\sqrt{N_{\rm g}}$, where $N_{\rm g}$ is the number of galaxies in the sample. The mode F^0 describes a Hubble-like flow in the space of the data set which is degenerated with the zero-point of the ITF relation. Here, we set $a^0 = 0$, which removes the Hubble-like flow from the gravity field, below. The best-fitting mode coefficients, a^j, the slope, γ, and the zero-point η_0 are found by minimizing the χ^2 statistic

$$\chi^2_{\rm ITF} = \sum_{i=1}^{N_{\rm g}} \frac{(\gamma M_{0i} + \gamma P_i + \eta_0 - \eta_i)^2}{\sigma^2_{\eta,{\rm int}}}, \tag{14}$$

where $\sigma_{\eta,{\rm int}}$ is the rms of the intrinsic scatter in η about the ITF relation, and $N_{\rm g}$ is the number of galaxies in the sample. Given the orthonormality condition, the solution to the equations $\partial\chi^2_{\rm ITF}/\partial a^j = 0$, $\partial\chi^2_{\rm ITF}/\partial\gamma = 0$ and $\partial\chi^2_{\rm ITF}/\partial\eta_0 = 0$ is straightforward. Thanks to the orthonormality condition, the covariance matrix $\langle\delta a_j \delta a'_j\rangle$ of the errors in a^j is diagonal with

$$\sigma_a = \langle(\delta a^j)^2\rangle^{1/2} = \frac{\sigma_{\eta,{\rm int}}}{\gamma}. \tag{15}$$

This lack of covariance of the errors in the coefficients is most rewarding as it makes the ITF error analysis exceptionally simple. Therefore, statistical assessment of the match between the data will be done at the level of the modes rather than the peculiar velocities. The interested reader will find details in ND95 and DNW96.

Downloaded from https://academic.oup.com/mnras/article-abstract/413/4/2906/965330
by guest
on 27 February 2018

3.3 The orthonormal basis functions

The choice of radial basis functions for the expansion of the modes can be made with considerable latitude. The functions should obviously be linearly independent, and close to orthogonal when integrated over volume. They should be smooth and close to a complete set of functions up to a given resolution limit. ND95 chose spherical harmonics Y_l^m for the angular wavefunctions and the derivatives of spherical Bessel functions for the radial basis functions, motivated by the desire to use functions which automatically satisfy potential theory boundary conditions at the origin and the outer boundary. That is, they chose

$$P(y,\theta,\phi) = \sum_{n=0}^{n_{\max}} \sum_{l=0}^{l_{\max}} \sum_{m=-l}^{m=l} \frac{a_{nlm}}{y} \left(j_l'(k_n y) - c_{l1} \right) Y_{lm}(\theta,\phi) . \quad (16)$$

The function $y(z)$ is designed to compress the distance scale, increasing the smoothing scale of the mode to deal with increased noise at large distances. For this analysis we use

$$y(z) = \sqrt{\log(1 + (z/z_s)^2)}, \quad (17)$$

where $z_s = 5000\,\mathrm{km\,s^{-1}}$. The constant c_{l1} is non-zero for the dipole term only and ensures that $P = 0$ at the origin, and is non-zero at the outer boundary. Details of how the orthogonalized functions $\tilde{F}_i^j$ are derived from this expansion are given in ND95.

The spherical harmonics are expanded to a maximum $n = 5$ and $l = 3$, except we delete the $n = 1$ mode for $l = 0$ as this mode can be confused with the false Hubble flow described in the next section. We also include an external quadruple, distinct from the internal quadruple, to describe the gravity induced by material at distances $cz > 10\,000\,\mathrm{km\,s^{-1}}$. Summing over the values of m, that makes a total of 72 modes fit towards reducing the χ^2 of equation (14). The use of $y(z)$ is designed to allow the radial resolution to degrade with distance; for example, the $n = 5$ modes have a wavelength in the radial direction of $3000\,\mathrm{km\,s^{-1}}$ at $cz = 8000\,\mathrm{km\,s^{-1}}$ and a wavelength of $1300\,\mathrm{km\,s^{-1}}$ at $cz = 1000\,\mathrm{km\,s^{-1}}$.

3.4 Expanding the 2MRS gravity field

In order to assess the match between the velocities by means of the expansion coefficients and to ensure that both fields are smoothed similarly, the 2MRS-predicted velocities v_g must also be described by an expansion over the basis functions used in the v_ITF model. Using the machinery for computing a gravity field described in Section 3.1, one can generate a linear theory predicted peculiar velocity v_g for any point in space as a function of its redshift for any value of β. We must ensure that the smoothing scales of the ITF and 2MRS-predicted peculiar velocities are matched to the same resolution. Therefore, we expand v_g in terms of the modes used in the velocity model. Because of the orthonormality, we can write the mode coefficients as

$$a_\mathrm{g}^j = 5 \sum_{i=1}^{N_\mathrm{g}} \log\left(1 - \frac{(v_{\mathrm{g},i} - H' c z_i)}{c z_i}\right) F_i^j, \quad (18)$$

where the H' term is a correction for the Hubble flow and the summation index i is restricted to be over the positions of the same galaxies in the ITF expansion.

This procedure will filter out fluctuations that are not described by the resolution of our basis functions. We do not include any mode such that $P_i =$ constant, which would be a pure Hubble flow. In the fitting for the ITF modes, pure Hubble flow is absorbed into a shift of the zero-point η_0 and the orthogonality is ensured. Within a given set of test points occupying a volume smaller than that used to define the gravity field, it is possible for v_g to have a non-zero value of Hubble flow H', which must be removed from v_g before we tabulate the mode coefficients. That is, we tabulate the mean Hubble ratio

$$H' = \frac{\sum_{k=1}^{N_\mathrm{g}} v_{\mathrm{g},k} c z_k}{\sum_{k=1}^{N_\mathrm{g}} v_{\mathrm{g},k}^2} \quad (19)$$

and subtract it from the predicted field v_g. This 'breathing mode' which mimics a Hubble flow is not trivial in amplitude, and can be a 10 per cent correction on the effective Hubble constant within simulated catalogues. This mode is cosmologically expected to a modest degree, but a bigger portion of the effect is caused by error in the determination of $\overline{n}$, which we estimate by assuming the weighted counts within $12\,000\,\mathrm{km\,s^{-1}}$ is the mean value.

3.5 Refinements of the ND95 functions

The Nusser & Davis (1995) reconstruction of the base functions can only provide a rough estimate of the spatial distribution of galaxies in the TF data. It does not guarantee that the signal-to-noise ratio in the filtered fields is uniform all over the sample. The ND95 expansion yields reliable TF velocities of nearby galaxies, but very noisy estimates at larger distances. Moreover, it is difficult to achieve a desired resolution as a function of redshift and to ensure equal resolutions in the radial and angular directions. The ND95 method expands the observed velocities in terms of harmonic functions, but the individual harmonic modes are not regularized and may acquire unrealistically large amplitudes, depending on the spatial coverage of the data.

We aim here at generating base functions which are themselves smoothed with a variable isotropic smoothing window designed to yield a constant signal-to-noise ratio in the estimated v_ITF. We construct these new basis functions with the help of the ND95 orthogonal functions denoted here by F^ND. Suppose a single radial velocity field, V_seed, with the appropriate variable smoothing has been found. We term V_seed the *seed* field as the new modes will stem from it. As will be described below this field will be chosen as the 2MRS-predicted velocity field, but any other field representing a viable velocity field could serve as V_seed. Given

$$P_{\mathrm{seed},i} = 5\log(1 - V_{\mathrm{seed},i}/cz_i) \quad (20)$$

(where i refers to galaxies in the TF sample) we expand $P_{\mathrm{seed},i}$ in base functions constructed according to ND95,

$$a_\mathrm{seed}^j = \sum_i P_{\mathrm{seed},i} F_i^{NDj} . \quad (21)$$

Here, the number of the modes F^{ND} is sufficiently large so that the inverse transformation $\sum_j a_\mathrm{seed}^j F_i^{NDj}$ reproduces $P_{\mathrm{seed},i}$. In practice we use about 1400 ND95 modes (we go to $l = 17$).

We then form additional fields, P_α, according to

$$P_{\alpha,i} = \sum_j \mathcal{R}_\alpha^j a_\mathrm{seed}^j F_i^{NDj} , \quad (22)$$

where $\mathcal{R}$ is a set of normally distributed random numbers with zero mean and standard deviation of unity. This reconstruction of the additional fields preserves the 'power' in the modal expansion and randomizes the phases. So far all these fields, $P_{\alpha,i}$, are unfiltered and may contain non-linear small-scale fluctuations. Therefore, we smooth all fields $P_{\alpha,i}$ according to

$$P_{\alpha,i}^\mathrm{smooth} = \sum_{\text{all galaxies}} P_{\alpha,i'} W(s_{i,i'}, R_{s,i'}) , \quad (23)$$

Downloaded from https://academic.oup.com/mnras/article-abstract/413/4/2906/965330
by guest
on 27 February 2018

where $s_{i,i'}$ is distance (in redshift space) between the galaxies i and i', and W is a Gaussian window of width $R_{s,i}$ which depends on the galaxy i. The smoothing width $R_{s,i}$ is tuned such that the expected error in the ITF velocity of galaxy i is $\sim$150 km s^{-1} and therefore it depends on the redshift and the local density of galaxies near i. The smoothing length at the positions of galaxies in the SFI++ sample is shown in Fig. 2; it varies roughly linearly with redshift, ranging from $1h^{-1}$ Mpc nearby up to $30h^{-1}$ Mpc for galaxies at redshifts $\sim$10000 km s^{-1}. The new basis functions are then obtained by orthonormalizing $P^{\rm smooth}_{\alpha,i}$. We refer to the new functions by the standard notation F^j_i, with F^1_i being the smoothed $P_{{\rm seed},i}$. These new modes will be used in the expansion given in equation (12). In Section 3.6, we describe how we determine the number of modes, $j_{\rm m}$, to be used in the expansion. The seed field $V_{\rm seed}$ could be constructed by interpolating any unfiltered cosmological velocity field on the positions of the galaxies in the SFI++ sample. Nevertheless, we could improve on this by constructing $V_{\rm seed}$ from the unfiltered 2MRS velocities given directly by the solution to equation (6). In practice, we use unfiltered $v_{\rm g}$ obtained with $\beta = 0.2$. The choice of $v_{\rm g}$ for $\beta = 0.2$ is arbitrary; the predicted field with any other β could be used. If the $V_{\rm seed} \sim v_{\rm g}$ and $v_{\rm ITF}$ both describe the same underlying velocity field, then the additional modes should mainly reflect the covariance of the errors between the two fields.

The flow patterns of nine of the modes are shown, respectively, in the nine panels in Fig. 3. The colour scheme throughout this paper is normal: red (blue) means outflowing (infalling), from the central point. We have extensively tested a broad variety of choices for the first mode. None of the results of the analysis reported is sensitive to this choice of the first mode. The figure shows that the higher-order modes exhibit smaller scale structures. This is a direct result of the orthogonolization processes. The jth + 1 mode has to be orthogonal to the all previous j modes. In order to achieve that, the orthogonalized jth + 1 will pick more of the small-scale structure.

3.6 The ITF scatter and the number of modes

Once the basis functions for the modal expansion are given, we proceed to solve for the coefficients a^j in $P_i = \sum a^j F^j_i$ by minimizing $\chi^2_{\rm ITF}$ in (14). The minimization is also performed, at the same time, with respect to the slope and zero-point of the ITF. The estimated slope is $\gamma = -0.1297 \pm 0.0015$ and -0.13 ± 0.0016, respectively, for 20 and 30 modes used in the flow model. The raw slope before fitting the model is $\gamma = -0.1267 \pm 0.0016$. The zero-point plays no role at all here, and we do not keep track of its estimated values. All estimated parameters, including a^j, are independent of the (assumed constant) intrinsic scatter $\sigma_{\eta,{\rm int}}$ in the ITF. The velocity model can be used to estimate the unknown value of $\sigma_{\eta,{\rm int}}$. Given the residual

$$\Delta\eta_i = \eta_i - (\gamma M_{0i} + \gamma P_i - \eta_0), \tag{24}$$

we approximate $\sigma_{\eta,{\rm int}}$ by

$$\sigma^2_\eta = \sum_i (\Delta\eta_i)^2 / N_{\rm d.o.f} \tag{25}$$

where

$$N_{\rm d.o.f} = N_{\rm g} - (j_{\rm m} + 2) \tag{26}$$

is the number of degrees of freedom taking into account that the minimization of $\chi^2_{\rm ITF}$ is done with respect to $j_{\rm m}$ coefficients plus the slope and zero-point of the ITF. This σ_η will decrease as the number of modes, $j_{\rm m}$, in the expansion is increased. If $j_{\rm m}$ is too large then the higher-order modes will be dominated by noise. If $j_{\rm m}$ is too small, then the model may miss significant components of the underlying true galaxy velocities.

The optimal range of $j_{\rm m}$ for our comparison can be seen by inspecting the behaviour of σ_η as a function of $j_{\rm m}$. The (blue) circles in the top panel of Fig. 4 show σ_η versus the number of modes for modes generated from the seed field $V_{\rm seed} = v_{\rm g}(\beta = 0.2)$ (see Section 3.5). Most of the reduction in σ^2_η is already achieved by the first mode. This is very encouraging since this means that $v_{\rm g}$ picks up a significant contribution of the velocities as described by the ITF data. It also means that both the 2MRS and the ITF data are likely to provide approximations to the underlying flow field. However, the 2MRS-predicted field $v_{\rm g}$ deviates from the underlying field by the presence of correlated errors in the reconstruction scheme. The inclusion of additional expansion modes in the ITF velocity model will dissolve these errors. The average reduction in the variance σ^2_η per mode becomes insignificant beyond $j_{\rm m} = 64$; the average reduction per mode for the first 64 modes is 10 times larger than that for the next 75 modes. An F-test also confirms that the reduction in the variance marginal beyond $j_{\rm m} = 64$. Hence, we will approximate $\sigma^2_{\eta,{\rm int}} = 0.0558$, the value acquired by σ_η for 64 modes in the velocity model. Therefore, the F-test argues that 64 is the maximum number modes needed to model the ITF.

The next step is to determine the minimum number of modes needed to describe the ITF flow assuming that $\sigma_{\eta,{\rm int}} = 0.0558$. To do so we tabulate $\chi^2_{\rm ITF}$ a function of $j_{\rm m}$ and compute the probability $Q = Q(\chi^2_{\rm ITF}|N_{\rm d.o.f.})$ that the value $\chi^2_{\rm ITF}$ is exceeded by chance (cf. section 6.2 in Press et al. 1992). The values of $\chi^2_{\rm ITF}/N_{\rm d.o.f.}$ and Q are represented as the (blue) circles, respectively, in the middle and bottom panels of Fig. 4. For $j_{\rm m} = 64$, we get $\chi^2_{\rm ITF}/N_{\rm d.o.f} = 1$ corresponding to $Q = 0.5$, in accordance with our choice of $\sigma_{\eta,{\rm int}}$. Without a velocity model, i.e. $j_{\rm m} = 0$, we get $(\chi^2_{\rm ITF}/N_{\rm d.o.f.}, Q) = (1.125, 3 \times 10^{-6})$. This exceedingly low Q rejects a vanishing velocity field with very high CL. Including the first mode alone gives a highly significant improvement: $(\chi^2_{\rm ITF}/N_{\rm d.o.f}, Q) = (1.031, 0.12)$. The hypothesis that $\chi^2_{\rm ITF}$ value corresponding to the first mode is obtained by chance is rejected only at the 0.12 CL. This is encouraging since the first-mode velocity field is proportional to the 2MRS-predicted velocities, $v_{\rm g}$ (for $\beta = 0.2$). For $j_{\rm m} = 30$ and 20 we get $(\chi^2_{\rm ITF}/N_{\rm d.o.f}, Q) = (1.01, 0.29)$ and $(1.014, 0.2)$, respectively.

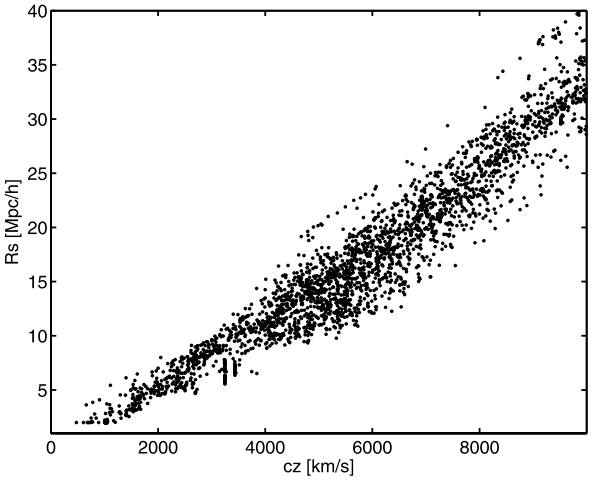

Figure 2. The width of the Gaussian smoothing Gaussian window versus galaxy redshifts in the SFI++ sample. The scatter reflects the angular variations in the density of galaxies.

Downloaded from https://academic.oup.com/mnras/article-abstract/413/4/2906/965330
by guest
on 27 February 2018

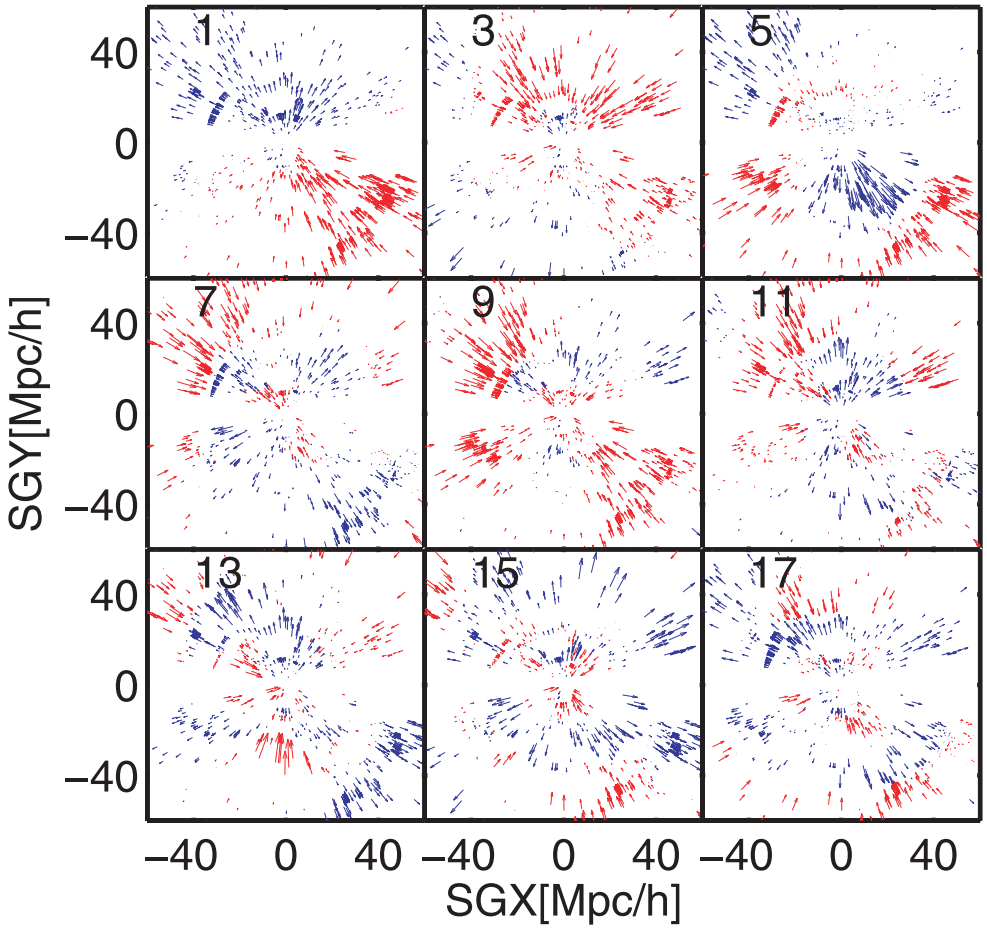

Figure 3. The flow patterns of nine modes for galaxies within $5h^{-1}$ Mpc of the supergalactic plane. The order of the mode is indicated in the corresponding panel.

For comparison with $V_{\rm seed} = v_{\rm g}$, the corresponding results for random choice of the seed field, $V_{\rm seed}$, are shown as the (red) crosses in the top and bottom panels of Fig. 4. With a random $V_{\rm seed}$, about 20 modes are needed to reduce σ_η to the level achieved by the single mode $v_{\rm g}$.

3.7 What is the purpose of the ITF machinery?

The expansion of the gravity field is conceptually very clean when computed in the LG frame (ND95). The Poisson-like equation for the 3D gravitational field has been solved as a sum over the spherical harmonic functions Y_{lm} times 1D functions of r that satisfy physically reasonable boundary conditions at the origin. For the purposes of the ITF solution, we furthermore quantize the radial solutions with quantum number n.

The ITF method is backward from the usual methodology of TF applications; one does not fit curves to the scatter of peculiar velocities. Instead, the χ^2 equation (14) is minimized by the addition of linear combinations of the orthonormal functions of n, l, m, where each describes a set of large-scale flow that satisfy the boundary conditions. Furthermore, we have endeavoured to form a first, 'seed', mode based on linear growth rate, but in which large-scale graininess is filtered out by the use of Fig. 2.

The individual galaxy's peculiar velocity enters by equation (11), with differential $dP_i \propto du_i/z_i$, and since the uncertainty of peculiar velocity u_i is proportional to redshift, the uncertainty of P_i is redshift independent. This means that each object is given equal weight in a fit, and our window function is therefore equivalent to the display of Fig. 5, which shows the positions of the SFI++ galaxies.

4 MOCK CATALOGUES AND ERROR ANALYSIS

As a measure of the agreement between the TF and predicted velocities by means of the corresponding expansion coefficients, $a_{\rm ITF}$ and $a_{\rm g}$, we will consider the χ^2 function

$$\chi^2 = \sum_{(j,k)=1}^{j_{\rm m}} \left(a_{\rm g}^j - a_{\rm ITF}^j\right) \left(\sigma_a^2 + \xi_{\rm g}\right)^{-1}_{j,k} \left(a_{\rm g}^k - a_{\rm ITF}^k\right) \ . \qquad (27)$$

The parameters α and β will be obtained by minimization of this function. The covariance of the residual, $a_{\rm ITF} - a_{\rm g}$, is the sum of the covariance matrices of the errors in the estimation of $a_{\rm ITF}$ and $a_{\rm g}$, respectively. Thanks to the orthonormality of the basis functions, the error covariance in the estimation of $a_{\rm ITF}$ is diagonal with constant terms $\sigma_a^2 = (\sigma_\eta/\gamma)^2$ (see Section 3.2 and DNW96). The matrix $\xi_{\rm g}$ represents the covariance of the errors in the determination of $a_{\rm g}$. The origin of these errors is as follows.

(i) Equation (6) is expected to predict reliable velocity fields only for small amplitude fluctuations. Small-scale non-linear deviations from linear theory inevitably leak to large scales.

Downloaded from https://academic.oup.com/mnras/article-abstract/413/4/2906/965330
by guest
on 27 February 2018

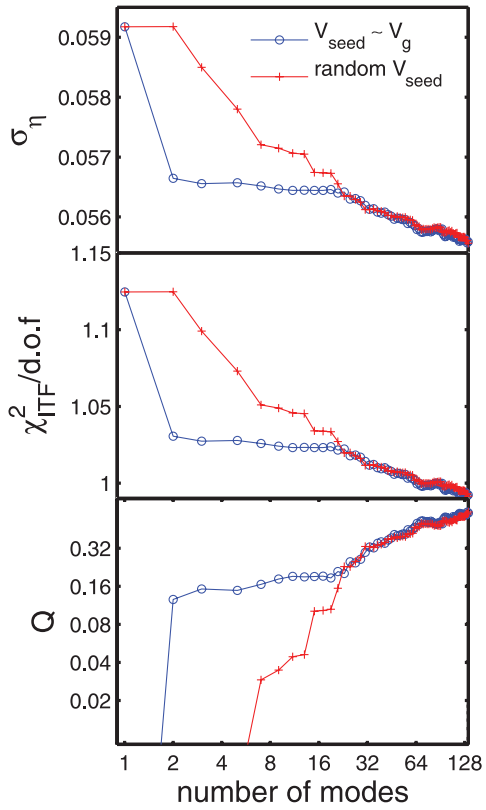

Figure 4. Top: the rms value, σ_η, of the ITF as a function of the number of modes used in the velocity model. Middle: $\chi^2_{\rm ITF}$ per degrees-of-freedom versus the number of modes. It is unity at 64 modes. Bottom: the probability that the $\chi^2_{\rm ITF}$ exceeds a certain value by chance, as a function of the number of modes. The chi-square is computed assuming an intrinsic scatter $\sigma_{\eta,\rm int} = 0.0558$. The value $Q = 0.5$ is achieved at 64 modes (see text for details).

(ii) The 2MRS is a finite number sampling of the underlying density field. This leads to 'shot-noise' errors in the estimation of the density field.

(iii) Small-scale random motions of galaxies, especially in groups and clusters, give rise to a smearing of the distribution of galaxies along the line of sight in redshift space.

(iv) There is a possible large-scale stochastic biasing (Dekel & Lahav 1999; Sigad, Branchini & Dekel 2000; Wild et al. 2005) between the galaxy distribution and the mass fluctuations.

The only way to achieve a reliable estimate of $\xi_{\rm g}$ taking into account all of these complicated errors is by means of mock catalogues designed to match the general properties of the 2MRS. A parent-simulated catalogue of the whole 2MASS catalogue has already been prepared (De Lucia & Blaizot 2007) by incorporating semi-analytic galaxy formation models in the Millennium simulation (Springel et al. 2005). From this parent catalogue we have drawn 15 independent mock 2MRS catalogues satisfying the following conditions.

(i) The 'observer' in each mock is selected to reside in a galaxy with a quiet velocity field within 500 km s^{-1}, similar to the observed Universe. That is, the central server sees only one cluster that has high enough peculiar velocities to result in negative redshifts. Recall that in the LG frame, the only galaxies with negative redshift are in the Virgo cluster.

(ii) The motion of the central galaxy is 500 to 700 km s^{-1}.

(iii) The density in the environment of the LG, averaged over a sphere of 400 km s^{-1} radius, is less than twice the normal.

Corresponding mock ITF catalogues were also prepared. A counts-in-cells statistics show that the distribution of galaxies in the mocks is unbiased relative to the dark matter, i.e. $b = 1$.

The preparation of the mocks for velocity reconstruction is done in the same way as the real data. Equation (6) is used to generate prediction of mock $v_{\rm g}$ with $\beta = f(\Omega, \Lambda)/b = 0.47$ corresponding to $b = 1$ and $\Omega = 0.25$ and $\Lambda = 0.75$ as in the Millennium simulation. The mean of the rms values of $v_{\rm g}$ in the mocks is 269 km s^{-1} and the standard deviation from this mean is 56 km s^{-1}. For contrast, the rms value of $v_{\rm g}$ derived from the 2MRS with $\beta = 0.35$ is 233 km s^{-1}.

To better illustrate the covariance between the residuals in the mocks, we plot in Fig. 4 the velocities $v_{\rm ITF}$ versus $v_{\rm g}$ for nine individual mocks. These are velocities expanded with 20 modes. Note the similarity between the structure of the distribution of points in the individual panels and the top panel in Fig. 6, showing $v_{\rm ITF}$ versus $v_{\rm g}$ (with $\beta = 0.35$) for the real data.

4.1 The error covariance matrix

The covariance matrix $\xi_{\rm g}$ is computed from the 15 mocks by projecting the correlation function, $\xi_{\rm P}$, of the residuals $\Delta P = P_{\rm itf} - P_{\rm g}$ on to the basis functions, where $P_{\rm itf} = 5\log(1 - v_{\rm ITF}/cz)$ and correspondingly for $P_{\rm g}$. That is

$$\xi_{\rm g}(j,k) = < \left(a^j_{\rm ITF} - a^j_{\rm g}\right)\left(a^k_{\rm ITF} - a^k_{\rm g}\right) >= \sum_{i,i'} F^j_i \xi_{\rm P}(i,i') F^k_{i'} \,, \tag{28}$$

where the summation in the last term on the right-hand side is over all data galaxies and F are the basis functions used for the real data. In this calculation, the $v_{\rm ITF}$ velocities are reconstructed from an ITF relation without adding the internal scatter of the TF relation. The reason is that the error in $a_{\rm ITF}$ resulting from the intrinsic scatter has a simple analytic form given by σ_a. The function $\xi_{\rm P}$ is computed from the 15 mocks as follows. Denote line-of-sight and projected separations in redshift space by $s_\parallel$ and $s_\perp$, respectively. For each mock we tabulate the average $\langle \Delta P_1 \Delta P_2 \rangle$ over pairs with separations defined by the grid. We then normalize this quantity by the variance of $v_{\rm ITF}$ (for zero ITF intrinsic scatter) in the corresponding mock. This is reasonable since the rms values of the velocity field vary considerably among the mocks and some of them are significantly different from the real data. To minimize this cosmic variance and to derive $\xi_{\rm g}$ given the observed rms value of the velocity, this normalization of $\langle \Delta P_1 \Delta P_2 \rangle$ for each mock is prudent. The average over all mocks is then computed and interpolated from the grid on to the actual pair separations in the TF catalogue to obtain the normalized $\xi_{\rm P}$. The normalized covariance matrix $\xi_{\rm g}$ is then computed according to (28) and scaled by a factor matching the velocity variance estimated from the observed $v_{\rm ITF}$.

5 THE RECONSTRUCTED VELOCITIES

This section presents a visual inspection of the fields, and assess the coherence of the residual $v_{\rm ITF} - v_{\rm g}$ by means of a velocity correlation analysis. The quantification of the agreement between the fields and the extraction constraints on α and β will be deferred to later sections.

Downloaded from https://academic.oup.com/mnras/article-abstract/413/4/2906/965330
by guest
on 27 February 2018

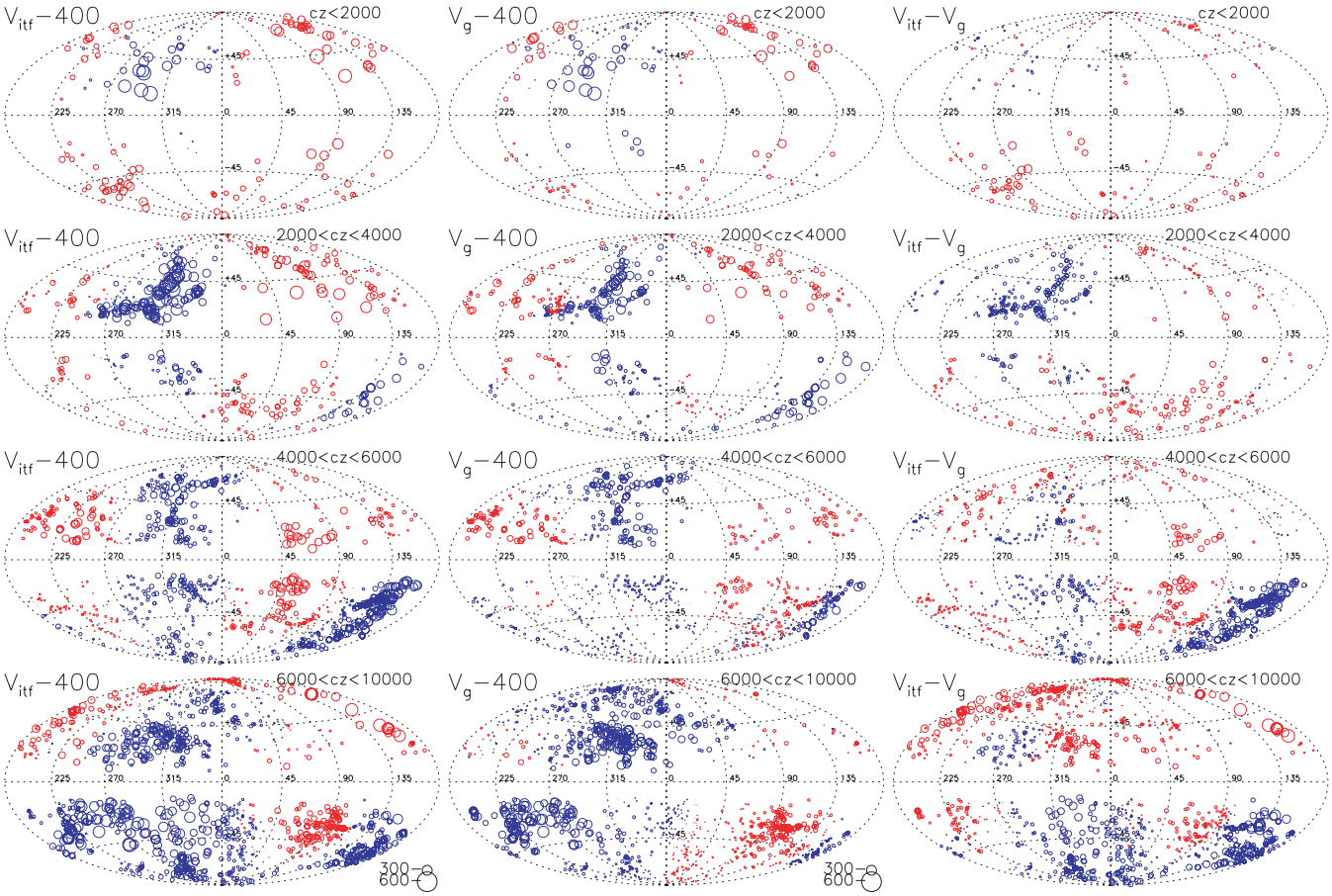

Figure 5. The derived peculiar velocities $v_{\rm ITF}$, $v_{\rm g}$ and $v_{\rm ITF} - v_{\rm g}$ of galaxies on aitoff projections on the sky in galactic coordinates. The rows correspond to galaxies with $cz < 2000$, $2000 < cz < 4000$, $4000 < cz < 6000\,{\rm km\,s^{-1}}$ and $6000 < cz < 10\,000\,{\rm km\,s^{-1}}$, respectively. The size of the symbols is linearly proportional to the velocity amplitude (see key to the size of the symbols given at the bottom of the figure). In order to better see the differences, a $400\,{\rm km\,s^{-1}}$ dipole, in the direction of the CMB dipole, has been subtracted from the $v_{\rm ITF}$ and $v_{\rm g}$ velocities. Note that $v_{\rm ITF} - v_{\rm g}$ is considerably smaller than $v_{\rm ITF}$ or $v_{\rm g}$, even for the most distant galaxies.

5.1 Visual inspection of the flows

Blue dots and red crosses of Fig. 6 show velocities expanded in 20 and 70 modes, respectively. In the bottom panel, $v_{\rm ITF}$ versus $v_{\rm g}$ from the mocks are shown. In mock $v_{\rm ITF}$ velocities are obtained from a fake ITF relation with an intrinsic slope $\gamma = -0.1$ and a scatter with $\sigma_\eta = 0.05$. For the sake of clarity only 400 randomly selected galaxies are shown in either panel. Further, each mock is represented by about 25 galaxies (randomly selected). The velocities are scaled by the corresponding rms value of $v_{\rm g}$ in the corresponding catalogue.

There is an excellent overall agreement between $v_{\rm ITF}$ and $v_{\rm g}$ for 20 modes, both in the real data and the mocks. A good agreement prevails even for 70 modes despite the clear enhanced noise contamination. In the real data, the rms of $v_{\rm ITF} - v_{\rm g}$ for 20 expansion modes is $99\,{\rm km\,s^{-1}}$, significantly smaller than $\sigma_{\rm g}$. For 70 modes the rms values of $v_{\rm g}$ and $v_{\rm ITF} - v_{\rm g}$ are $238\,{\rm km\,s^{-1}}$ and $231\,{\rm km\,s^{-1}}$, respectively. Both panels show clear structures in the distribution of points, implying strong covariance between the residuals, $v_{\rm ITF} - v_{\rm g}$, in the real, or mock, data. Because the bottom panel represents random selections of galaxies from all the mocks, the covariance pattern between the velocities is diluted in the distribution of points. The covariance pattern is, however, clear in Fig. 7 where scatter velocity plots for a few mocks are shown individually.

In the aitoff projections in Fig. 5 we plot the TF peculiar velocities, $v_{\rm ITF}$ and the derived gravity modes, $v_{\rm g}$, for galaxies in redshift shells, $cz < 2000$, $2000 < cz < 4000$, $4000 < cz < 6000$ and $6000 < cz < 10\,000\,{\rm km\,s^{-1}}$. The projections are in galactic coordinates centred on l, $b = 0$ and with $b = 90$ at the top. Figs 5 and 8 show $v_{\rm g}$ with $\beta = 0.35$. The rightmost plots are the residuals $v_{\rm ITF} - v_{\rm g}$. The key point is to note that the residuals are small for the entire sky and have amplitude that is constant with redshift. The amplitude and coherence of the residuals $v_{\rm ITF} - v_{\rm g}$ is the same as for the mock catalogues in Fig. 8, where, for example, the lower-right picture shows $v_{\rm ITF} - v_{\rm g}$ for a mock catalogue. It is not very dissimilar from the real plot of $v_{\rm ITF} - v_{\rm g}$ in the upper right, demonstrating the feasibility of the entire method.

Note the quadrupole pattern for $cz < 4000\,{\rm km\,s^{-1}}$ in Figs 5 and 8, visible after $400\,{\rm km\,s^{-1}}$, has been subtracted from the flow. This has been previously noted by Haugbølle et al. (2007) on the basis of the flows detected in 133 SNe. The quadrupole is the typical pattern observed in N-body simulations and is the principle mode of collapse to a 1D structure.

There is amazingly overall good agreement between the large-scale motions as described by $v_{\rm ITF}$ and $v_{\rm g}$. The residual velocities are coherent over large scales but they are clearly of smaller amplitude than $v_{\rm ITF}$ and $v_{\rm g}$. Note that residuals shown in $v_{\rm ITF} - v_{\rm g}$, particularly visible in the shell $6000 < cz < 10\,000\,{\rm km\,s^{-1}}$, are dominated by

Downloaded from https://academic.oup.com/mnras/article-abstract/413/4/2906/965330
by guest
on 27 February 2018

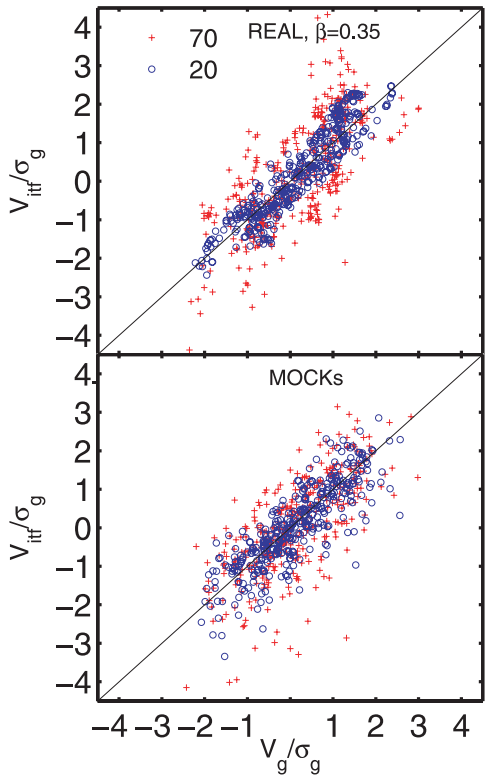

Figure 6. The peculiar velocities $v_{\rm ITF}$ versus $v_{\rm g}$ of galaxies in the real data (top) and the mocks (bottom) for 20 and 70 expansion modes, as indicated in the figure. The real $v_{\rm g}$ has been reconstructed with $\beta = 0.35$ and $\alpha = 0$. Velocities of about 400 randomly selected galaxies are plotted in each panel where each mocks is represented by about 25 galaxies. All velocities in the top panel are normalized by the rms value, $\sigma_{\rm g} = 233\,{\rm km\,s^{-1}}$ of $v_{\rm g}$, while velocities in the bottom panel are normalized by the rms value of $v_{\rm g}$ of their corresponding catalogues.

$l = 4$, because the fit for the reduction of the TF χ^2 is limited at $l = 3$ modes.

5.2 Correlations

The residuals, both in the real and in mock data, have error fields, $v_{\rm ITF} - v_{\rm g}$, that show large regions of coherence. To address the significance of these errors, we show in Fig. 9 the velocity correlation function (Gorski et al. 1989), defined as

$$\Psi(s;u) = \frac{\sum_{\rm pairs} u_1 u_2 \cos\theta_{12}}{\sum_{\rm pairs} \cos^2\theta_{12}}, \qquad (29)$$

where the sum is over all pairs, 1 and 2, separated by vector distance $\boldsymbol{s}_{12}$ (in redshift space), θ_{12} is the angle between points 1 and 2, and u is either $v_{\rm ITF}$ (dashed red) or $v_{\rm ITF} - v_{\rm g}$ (red for data, blue for 15 mock catalogues). At small lags for the real data, the function $\Psi(r;\, v_{\rm ITF} - v_{\rm g})$ is a factor of 3 less than $\Psi(s;\, v_{\rm ITF})$, about the same as for the mock catalogues. Note how the large coherence of $v_{\rm ITF}$ is enormously diminished in $\Psi(s > 2000\,{\rm km\,s^{-1}};\, v_{\rm ITF} - v_{\rm g})$. This shows that the coherence seen in the residual field (Fig. 9) is expected and is not a problem. The large-scale drift of a sample is demonstrated by the persistent amplitude of Ψ beyond $\approx 60 - 80\,{\rm Mpc}$.

The bottom panel of Fig. 9 shows velocity correlations for 15 mock catalogues where the actual velocity, $v_{\rm true}$, generated in the N-body code and then smoothed with the 20 mode expansion can be compared to either $v_{\rm ITF}$ or $v_{\rm g}$. Note that the raw velocities, $v_{\rm itf}$ (red), have enormous correlation that reaches large lag, while the correlations, $(v_{\rm true} - v_{\rm ITF})$, (blue) are extremely small. This is because the only difference with $v_{\rm true}$ is the Gaussian error in $\Delta\eta = 0.05$ that affects $v_{\rm ITF}$. The blue curves show this error is not a problem, because the mode expansions are insensitive to Gaussian noise in the 2500 galaxies, i.e. they are essentially perfect. This demonstrates that even though the TF noise is as large as for the actual data, the ability to find the correct flow, when characterized by only 20 numbers, is intact.

Note also that the auto-covariance of $(v_{\rm true} - v_{\rm g})$ (dot–dashed curves) is also greatly reduced from that of $v_{\rm ITF}$. Recall that $v_{\rm g}$ assumes linear theory estimated from the distribution of 20 000 galaxies. Occasionally, the correlations are badly mistaken, when a large cluster (much larger than Virgo) is in the foreground and complicates the difference between physical and redshift-space separations, but $v_{\rm g}$ is always an excellent approximation to the TF velocity.

6 THE CONSTRAINTS ON α, β

Equipped with the error covariance matrices, we proceed to minimize χ^2 in equation (27) with respect to α and β. We shall present detailed results for α and β for fields expanded in 20 modes and 30 modes.

The minimization is done by computing χ^2 on a grid of values in the plane α and β. At the minimum point $\chi^2 = \chi^2_{\rm min} = 21.5$ which is very reasonable given that the standard deviation from the expected value of 22 (20 mode coefficients plus TF slope and zero-point) is $\sim\sqrt{44} \approx 7$ (Press et al. 1992).

Fig. 10 shows the difference $\Delta\chi^2 = \chi^2 - \chi^2_{\rm min}$ as a function of β for three fixed values of α, as indicated in the figure. The horizontal lines indicate 68 per cent and 95 per cent CLs. Fig. 12 is a contour plot of $\Delta\chi^2$ in the plane of α and β.

The higher frequency basis functions should probe smaller scales. Hence, if our assumption of linear bias which is independent of scale is valid, then varying the number of modes, $j_{\rm m}$, should yield consistent constraints on β. Fig. 11 shows the best-fitting β (thick red curve) and the corresponding 95 per cent (2σ) CLs (thin blue solid lines) versus the number modes in the expansion, for $\alpha = 0$. The circles show the 'differential' best-fitting β obtained from a single mode as a function of the order of the mode. The 2σ error bars on this differential β are significantly enhanced beyond the second-order mode. A few points lie at the ends of the error bars corresponding to best-fitting β obtained at either 0.05 or 0.7 which are the bounds of the range of β values used in the 2MRS reconstruction. There is a hint that β declines with increasing $j_{\rm m}$ but this is completely dominated by the noise. This figure shows clearly that we get consistent constraints on β (the red curve) when varying the number of modes in the expansion. Further, it shows that most of the signal is contained in the very few first modes.

7 DISCUSSION

The analysis reported demonstrates a good match between the 2MRS-predicted and TF-observed velocities. The analysis is unique in several respects. First, it completely avoids dealing with covariance matrices of errors in the velocities estimated from the TF sample, Secondly, it uses elaborate mock galaxy catalogues to compute the error covariance in the predicted velocities from the redshift survey. Thirdly, the TF and predicted velocities are filtered in a very similar fashion, taking special care to minimize the effects of noise

Downloaded from https://academic.oup.com/mnras/article-abstract/413/4/2906/965330
by guest
on 27 February 2018

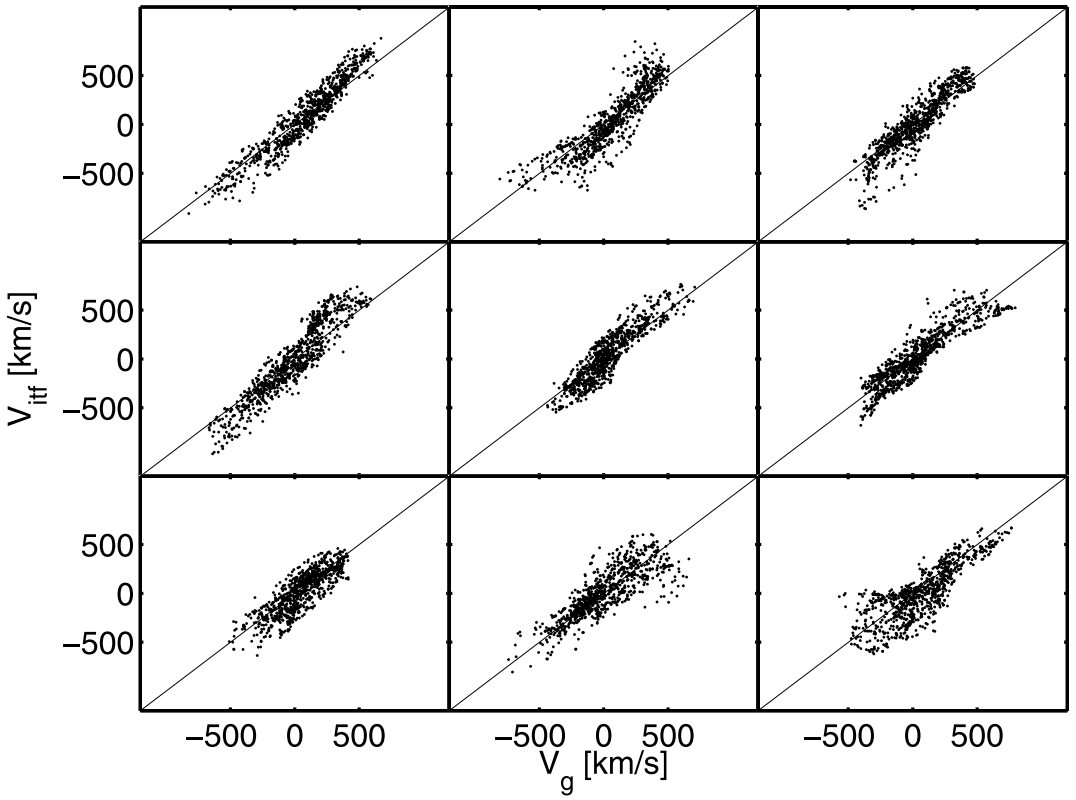

Figure 7. Scatter plots of $v_{\rm ITF}$ versus $v_{\rm g}$ (expanded in 20 modes) for galaxies in nine mock catalogues. About 800 galaxies are plotted for each mock.

in the comparison. In this analysis faint galaxies with $M > -20$ are excised from the TF catalogue since they systematically show strong deviations from the linear TF relation.

The comparison yields $\beta = f/b = 0.33 \pm 0.04$ (1σ error). The quoted error is not actually far from the limit of what the current data can constrain in the absence of any errors on the 2MRS predicted velocities.[2] A moderate reduction of the errors by a factor of 2 requires a significant enlargement in the number of peculiar velocity measurements by a factor of 4, which could be done if dedicated time is available, but the TF samples already use the best local galaxies. Going to larger distance is not the answer, as the error of a peculiar velocity increases linearly with the distance, and the 2MRS density field becomes very dilutely sampled. Two surveys, WALLABY, to be undertaken by the ASKAP telescope in Western Australia, and ALFALFA, an ongoing project at Arecibo, will hopefully produce good TF data for $cz < 12\,000\,{\rm km\,s^{-1}}$. Another strategy would involve peculiar velocities inferred from more precise distance indicators than the TF relation. SNe and surface brightness fluctuation techniques are likely candidates, but such measurements are available for a much smaller number of galaxies. Larger samples of local SNe are turning out to have increased errors (Ganeshalingam, private communications), significantly larger than previously measured (e.g. Riess et al. 1997).

The good match between the gravity and velocity fields implies that they probe the same underlying potential field within the framework of the gravitational instability paradigm for structure formation. The agreement is achieved assuming a linear biasing relation between mass and galaxies on large scales. Linear biasing is consistent with theoretical predictions (e.g. Kauffmann, Nusser & Steinmetz 1997) for the large-scale clustering of galaxies. Further, no scale-dependent biasing seems to be required by the velocity comparison. However, the theoretically expected scale dependence of the bias factor (e.g. Peacock & Smith 2000; Desjacques et al. 2010) is well below the level which can be probed by the velocity comparison carried out here. There is also no clear indication for a scale-dependence bias from the observed galaxy clustering on the relevant scales (e.g. Verde et al. 2002).

DNW96, which compared the predicted velocities from the *IRAS* 1.2 Jy redshift surveys and the MARK III TF data, revealed systematic discrepancies that could not be attributed to errors in the data and the reconstruction methods. Inspection of the flow fields obtained in the current work with the those presented in DNW96 (see their figs 9–13) clearly shows that the problem lies in the MARK III data set. The velocity fields predicted from the *IRAS* and 2MRS surveys have similar patterns which grossly deviate from MARK III but are in accordance with SFI++. The 2MRS has all the attributes that one would want for estimating the gravity field including a very weak bias. The survey was done by an instrument that was photometrically stable, which is important to avoid large-scale drifts in the derived gravity field. The survey is far superior to the *IRAS*

[2] In the absence of gravity errors and for β close to the best-fitting value β_0, the χ^2 function is approximated as

$$\chi^2 = \sum_j \left[a^j_{\rm ITF} - B(\beta) a^j_{\rm g0}\right]^2 / \sigma_a^2,$$

where $a^j{}_{\rm g0}$ correspond to reconstruction with $\beta = \beta_0$ and $B = (\beta/\beta_0)(1 + 1.5\beta_0)/(1 + 1.5\beta)$ approximates the dependence of $v_{\rm g}$ on β (in contrast to the dependence β/β_0 in reconstruction from galaxy distribution in real space). The 1σ error in B is $\sigma_{\rm a}/\sqrt{\sum_j (a^j_{\rm g0})^2} \approx 0.06$, where we took $\sigma_{\rm a} = \sigma_\eta/\gamma = 0.43$ and $\sum_j (a^j_{\rm g0})^2 = 52$ as given from the solution with $\beta = 0.35$. This error in B translates into an error of 0.03 in β which is close to the error obtained with the full analysis.

Downloaded from https://academic.oup.com/mnras/article-abstract/413/4/2906/965330
by guest
on 27 February 2018

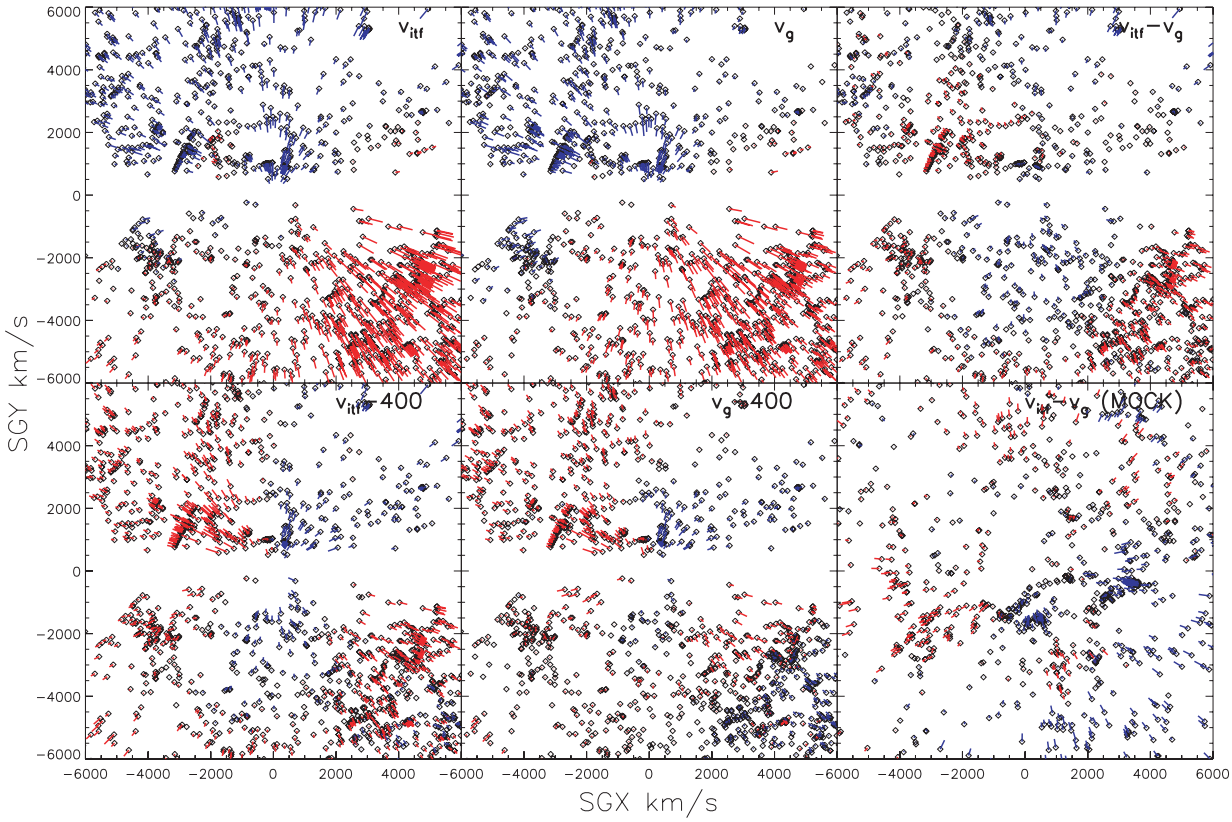

Figure 8. Supergalactic plane projection, $|SGB| < 30$, of the derived flows. To better see the differences in the plots, a dipole of 400 km s^{-1} towards the CMB pole has been subtracted from the fields, and is shown in the bottom left and bottom centre. A quadruple velocity is now visible in the plots. The points are drawn at the estimated distance of an SFI++ galaxy, and the line, blue or red, is drawn to the galaxy's redshift. In other words, the length of the arrow is the peculiar velocity. The lower-right plot shows $v_{\rm ITF} - v_{\rm g}$ for a mock catalogue, and the upper right shows $v_{\rm ITF} - v_{\rm g}$ for the data. They have very similar degrees of coherence.

survey, the first full sky galaxy survey, which detected galaxies at 60 μm, a sign of star formation and not a good indicator of mass. However, that survey led to sensible results, and was not at fault for the disagreement 15 yr ago.

Radburn-Smith, Lucey & Hudson (2004) compared the predicted velocities from the *IRAS PSCZ* survey to measured peculiar velocities of SNe. They found a best-fitting $\beta_{IRAS} = f/b_{IRAS} = 0.55 \pm 0.06$. The lower value of β derived in our work could be due to a difference in the biasing factor between 2MRS and the *IRAS* galaxies, but we also emphasize that our estimation of the error in the predicted velocities should be more reliable as it is based on realistic mock catalogues. Pike & Hudson (2005) performed a comparison of the 2MRS predicted velocities with direct velocity measurements from three different samples, including 836 SFI++ galaxies within $cz = 5000$ km s^{-1}. Their analysis yields $\beta = 0.55 \pm 0.05$ for the comparison of gravity with the SFI++. They derive $\Omega = 0.55 \pm 0.05$, inconsistent with our result at more than the 2.5σ level. However, they did not calibrate their methods with advanced mock catalogues nor included the expected covariance of the predicted velocities.

Lavaux et al. (2010) employed a sophisticated version of the non-linear MAK reconstruction method (Frisch et al. 2002b) to compare the 2MRS-predicted velocities with the 3 K velocity catalogue (Tully et al. 2008) of 1791 galaxies with redshifts <3000 km s^{-1}. They derive $\Omega = 0.31 \pm 0.05$, corresponding to $\beta \sim 0.52$. However, as they point out their error analysis is incomplete. Their method is promising as it takes into account non-linear effects. Nevertheless, they do not account for the covariance of the errors in their smoothed observed velocities and predicted velocities.

Both Pike & Hudson (2005) and Lavaux et al. (2010) use iterative schemes based on Yahil et al. (1991) for deriving the peculiar velocities from redshift surveys. These schemes rely on a relation between the peculiar velocity and density in real space. At any iteration, this relation is solved for new peculiar velocity given real-space coordinates obtained from the observed redshifts by subtracting the old peculiar velocities derived in the previous iteration. We caution here that the these schemes are intrinsically biased: error in velocities used to estimate the distances will yield a biased density field in real space (see the Appendix for details). Hence, the estimation of the velocity field is actually done from a biased distribution in real space. The bias produces an undesired smoothing of density field along the radial direction. The smoothing width (in km s^{-1}) is equal to the rms random error in the velocities ∼200–300 km s^{-1} (Branchini, Eldar & Nusser 2002; Nusser & Branchini 2000). Therefore, the bias is more pronounced in non-linear methods which aim at probing small scales.

Checks to find the best way of estimating the gravity field did not lead to improvements. Weighting the galaxy maps by the 2MRS luminosity led to a worse agreement, and recall that 2MRS is selected in K band, which is closest to a measure of the stellar mass. Giving the elliptical galaxies double weight, as indicated by lensing analysis (Mandelbaum et al. 2006), did not improve the agreement. This in itself is not too surprising, because on large scale the 2MRS

Downloaded from https://academic.oup.com/mnras/article-abstract/413/4/2906/965330
by guest
on 27 February 2018

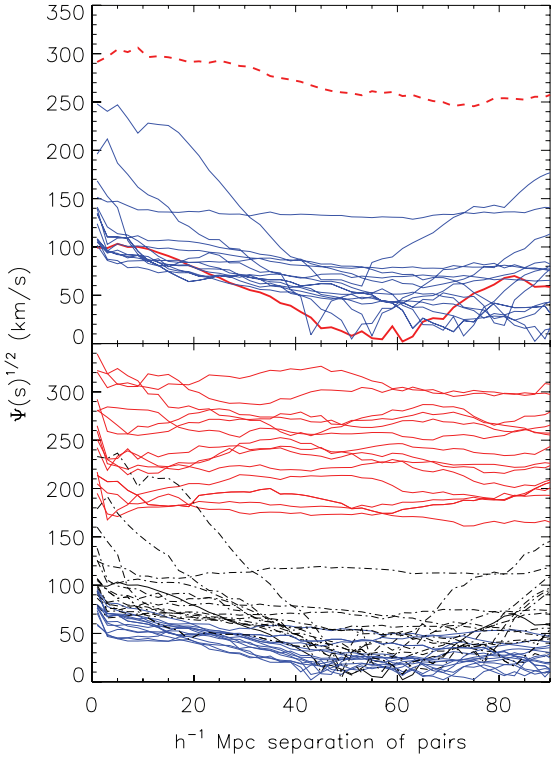

Figure 9. Top: the velocity correlation of the real data and 15 mock catalogues. The dashed red and solid red curves are, respectively, the correlations of $v_{\rm ITF}$ and $v_{\rm ITF} - v_{\rm g}$ in the real data. The blue lines are each correlations of $v_{\rm ITF} - v_{\rm g}$ for the mock catalogues. Bottom: velocity correlations for 15 mock catalogues. The red curves are the velocity of $v_{\rm itf}$, the dot–dashed curves show the correlation of $(v_{\rm true} - v_{\rm g})$, and the blue curves correspond to $v_{\rm true} - v_{\rm itf}$. Both $v_{\rm true}$ and $v_{\rm g}$ are first smoothed with the 20 mode expansion before the auto-covariance is computed. Note that the correlation of $v_{\rm ITF} - v_{\rm g}$ is only slightly worse than the correlation of $v_{\rm true} - v_{\rm gs}$, showing that the velocity reconstruction dominates the errors. Note also that we are plotting the square root of the velocity correlation Ψ.

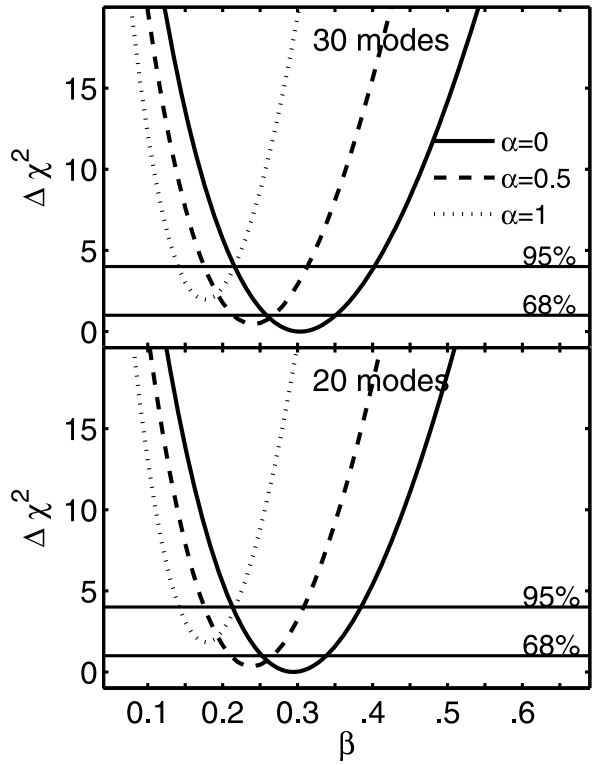

Figure 10. The difference $\Delta\chi^2 = \chi^2 - \chi^2_{\rm min}$ versus β computed for three values of α, as indicated in the figure. Horizontal lines mark the 68 per cent and 95.4 per cent CLs.

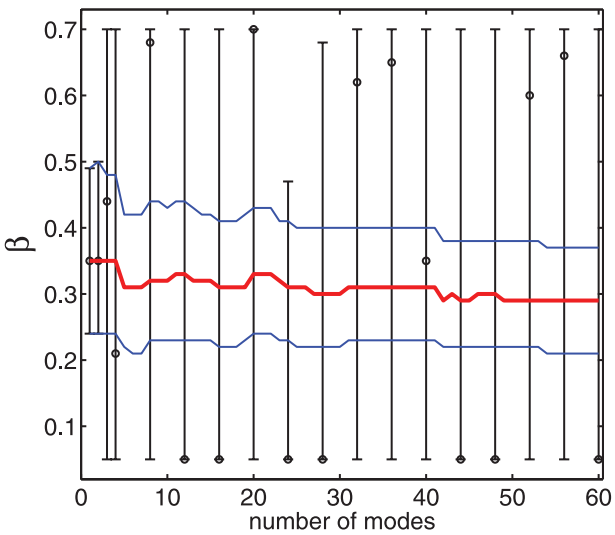

Figure 11. The thick solid red line is best-fitting β as a function of the number of modes in the velocity model, for $\alpha = 0$. The thin blue lines mark the 95 per cent CL on the best fit. The circles denote the 'differential' best-fitting β obtained with the single jth mode. After the first four modes, only one in four modes are represented. The error bars attached to the circles correspond to 95 per cent CLs on the differential best fit.

survey is dominated by spiral galaxies. It seems that the galaxies brighter than $M_* + 2$ are each surrounded by a dark matter halo that has the same mass on average. There is no hint that the dark matter mass is larger if the luminosity is increased.

Using our estimate for β we can constrain the amplitude of mass fluctuations. As a measure of the amplitude we consider the rms of density fluctuations in spheres of $8h^{-1}$ Mpc in radius, denoted by σ_8 and σ_{8g} for the mass and galaxy distributions, respectively. Adopting $\Omega = 0.266$ (Larson et al. 2010) gives $f(\Omega, \Lambda = 1 - \Omega) = 0.483$ (Linder 2005). Comparing this to our result $\beta = f/b = 0.33 \pm 0.04$ (1σ error) we get a bias factor $b = 1.46 \pm 0.20$ between the dark matter and the 2MRS galaxy distribution. Taking $\sigma_{8g} = 0.97 \pm 0.05$ (Westover 2007; Reid et al. 2010) yields $\sigma_8 = \sigma_{8g}/b = 0.65 \pm 0.11$ for the underlying mass density field, marginally consistent with the latest *Wilkinson Microwave Anisotropy Probe* (*WMAP*) results (Larson et al. 2011) of $\sigma_8 = 0.8 \pm 0.03$ (see also Jarosik et al. (2010)).

8 CONCLUSIONS

We summarize the major conclusions of our work.

(i) After a detailed examination of the 2MRS and SFI++ catalogues, we find the local gravity field to be a fine predictor of the local velocity field. Such a conclusion is a comfort for linear perturbation theory in an expanding universe and was certainly expected. It is interesting that the counts of galaxies give the best possible gravity field, reinforcing the old idea that the mass of the

Downloaded from https://academic.oup.com/mnras/article-abstract/413/4/2906/965330
by guest
on 27 February 2018

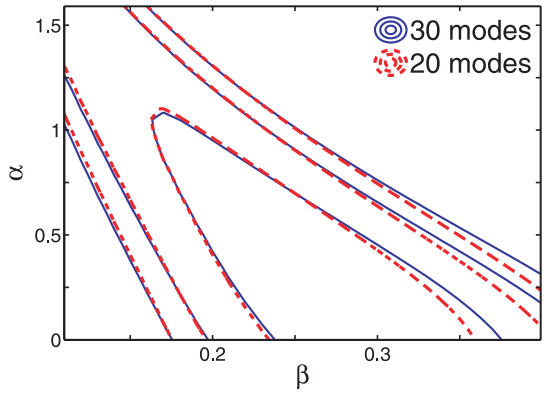

Figure 12. Contour plot of $\Delta\chi^2$ in the plane of α and β. The contours are 2.3, 6.17 and 9.2 corresponding to CLs of 68 per cent, 95.4 per cent and 99 per cent, respectively.

halo around a galaxy is not very well correlated with the luminosity of that galaxy.

(ii) We see no evidence that the dark matter does not follow the galaxy distribution, and is consistent with constant bias on large scales. There is no evidence for a non-linear bias in the local flows. A smooth component to the Universe is not something testable with these methods.

(iii) Linear perturbation theory appears to be adequate for the large scales tested by our method.

(iv) The solution favours $\alpha = 0$, no correlation between luminosity and mass, and $\beta = 0.33 \pm 0.04$, which is consistent, but more than twice as tight as Erdoğdu et al. (2006b). Using the derived Ω from *WMAP* (Jarosik et al. 2011) leads to an estimate $\sigma_8 = 0.65 \pm 0.10$, deviant from *WMAP*'s reports at the 1.5σ level.

(v) Our estimate of σ_8 gives the most precise value at $z \sim 0$ and is useful for tests of the growth rate and Dark Energy.

(vi) The velocity-gravity comparison measures the acceleration on scales up to 30–50 Mpc and since we derived a similar value of β as for clusters of galaxies, we conclude that dark matter appears to fully participate in the clustering on scales of a few megaparsec and larger.

(vii) We find no evidence for large-scale flows such as reported by, for example, Hudson et al. (1999), Hudson & Ebeling (1997) and Feldman et al. (2010). Note that our analysis has not used the CMBR dipole, but we see a velocity field that is fully consistent with those previously reported (Erdoğdu et al. 2006a,b; Erdoğdu & Lahav 2009), which are consistent with the CMBR dipole radiation. We see no evidence that the dipole in the CMBR is produced by anything other than our motion in the Universe.

ACKNOWLEDGMENTS

We are all grieving over the untimely death of John Huchra, an old dear friend who first collaborated on papers describing the CfA1 survey. We are indebted to him for his contribution to this research, including being responsible for completion of the 2MRS and for pushing the observations to low galactic latitude.

We thank Enzo Branchini for a careful reading of the manuscript. MD acknowledges the support provided by the NSF grant AST-0807630. The majority of this research was carried out at the MPA, Garching, when MD was supported by a Humboldt fellowship. AN thanks the MPA for the hospitality. This work was supported by The Israel Science Foundation (grant No.203/09), the German-Israeli Foundation for Research and Development, the Asher Space Research Institute and by the Winnipeg Research Fund. KLM acknowledges funding from the Peter and Patricia Gruber Foundation as the 2008 Peter and Patricia Gruber Foundation International Astronomical Union Fellow, from a 2010 Leverhulme Trust Early Career Fellowship and from the University of Portsmouth and SEPnet (www.sepnet.ac.uk). The Millennium Simulation data bases used in this paper and the web application providing online access to them were constructed as part of the activities of the German Astrophysical Virtual Observatory.

REFERENCES

Aaronson M., Huchra J., Mould J., Schechter P. L., Tully R. B., 1982, ApJ, 258, 64
Abate A., Erdoğdu P., 2009, MNRAS, 400, 1541
Abazajian K. N. et al., 2009, ApJS, 182, 543
Bernardeau F., Juszkiewicz R., Dekel A., Bouchet F. R., 1995, MNRAS, 274, 20
Borgani S., da Costa L. N., Zehavi I., Giovanelli R., Haynes M. P., Freudling W., Wegner G., Salzer J. J., 2000, ApJ, 119, 102
Branchini E. et al., 2001a, MNRAS, 326, 1191
Branchini E. et al., 2001b, MNRAS, 326, 1191
Branchini E., Eldar A., Nusser A., 2002, MNRAS, 335, 53
Bridle S. L., Zehavi I., Dekel A., Lahav O., Hobson M. P., Lasenby A. N., 2001, MNRAS, 321, 333
Chodorowski M. J., Nusser A., 1999, MNRAS, 309, L30
Colless M. et al., 2003, preprint (astro-ph/0306581)
Croft R. A. C., Gaztanaga E., 1998, ApJ, 495, 554
da Costa L. N., Nusser A., Freudling W., Giovanelli R., Haynes M. P., Salzer J. J., Wegner G., 1998, MNRAS, 299, 425
Davis M., Huchra J., Latham D. W., Tonry J., 1982, ApJ, 253, 423
Davis M., Nusser A., Willick J. A., 1996, ApJ, 473, 22 (DNW96)
de Lapparent V., Geller M. J., Huchra J. P., 1986, ApJ, 302, L1
De Lucia G., Blaizot J., 2007, MNRAS, 375, 2
Dekel A., Lahav O., 1999, ApJ, 520, 24
Dekel A., Bertschinger E., Yahil A., Strauss M. A., Davis M., Huchra J. P., 1993, ApJ, 412, 1
Desjacques V., Crocce M., Scoccimarro R., Sheth R. K., 2010, Phys. Rev. D, 82, 3529
Enßlin T. A., Frommert M., Kitaura F. S., 2009, Phys. Rev. D, 80, 105005
Erdoğdu P., Lahav O., 2009, Phys. Rev. D, 80, 043005
Erdoğdu P. et al., 2006a, MNRAS, 373, 45
Erdoğdu P. et al., 2006b, MNRAS, 368, 1515
Feldman H. A., Watkins R., 2008, MNRAS, 387, 825
Feldman H. A., Hudson M. J., Watkins R., 2008, preprint (arXiv e-prints)
Feldman H. A., Watkins R., Hudson M. J., 2010, MNRAS, 407, 2328
Fisher K. B. et al., 1995a, ApJS, 100, 69
Fisher K. B., Lahav O., Hoffman Y., Lynden Bell D., Zaroubi S., 1995b, MNRAS, 272, 885
Freudling W. et al., 1999, ApJ, 523, 1
Frisch U., Matarrese S., Mohayaee R., Sobolevski A., 2002a, Nat, 417, 260
Frisch U., Matarrese S., Mohayaee R., Sobolevski A., 2002b, Nat, 417, 260
Giovanelli R., Haynes M. P., Salzer J. J., Wegner G., da Costa L. N., Freudling W., 1994, AJ, 107, 2036
Giovanelli R., Haynes M. P., Salzer J. J., Wegner G., da Costa L. N., Freudling W., 1995, AJ, 110, 1059
Giovanelli R., Haynes M. P., Herter T., Vogt N. P., Wegner G., Salzer J. J., da Costa L. N., Freudling W., 1997a, AJ, 113, 22
Giovanelli R., Haynes M. P., Herter T., Vogt N. P., da Costa L. N., Freudling W., Salzer J. J., Wegner G., 1997b, AJ, 113, 53
Gorski K. M., Davis M., Strauss M. A., White S. D. M., Yahil A., 1989, ApJ, 344, 1
Gurovich S., Freeman K., Jerjen H., Staveley-Smith L., Puerari I., 2010, ApJ, 140, 663

Downloaded from https://academic.oup.com/mnras/article-abstract/413/4/2906/965330
by guest
on 27 February 2018

Haugbølle T., Hannestad S., Thomsen B., Fynbo J., Sollerman J., Jha S., 2007, ApJ, 661, 650
Haynes M. P., Giovanelli R., Chamaraux P., da Costa L. N., Freudling W., Salzer J. J., Wegner G., 1999, ApJ, 117, 2039
Huchra J. et al., 2005, in Colless M., Staveley-Smith L., Stathakis, eds, IAU Symp. Vol. 216, Maps of the Cosmos. Astron. Soc. Pac., San Francisco, p. 170
Hudson M. J., Ebeling H., 1997, ApJ, 479, 621
Hudson M. J., Dekel A., Courteau S., Faber S. M., Willick J. A., 1995, MNRAS, 274, 305
Hudson M. J., Smith R. J., Lucey J. R., Schlegel D. J., Davies R. L., 1999, ApJ, 512, L79
Jaffe A. H., Kaiser N., 1995, ApJ, 455, 26
Jarosik N. et al., 2011, ApJS, 192, 14
Jarrett T. H. et al., 2000, ApJ, 119, 2498
Jones H., Saunders W., Colless M., Read M., Parker Q., Watson F., Campbell L., 2005, in Fairall A. P., Woudt P. A., eds, ASP Conf. Ser. Vol. 329. Nearby Large-Scale Structures and the Zone of Avoidance. The 6dF Galaxy Survey: First Data Release. Astron. Soc. Pac., San Francisco, p. 11
Jones D. H. et al., 2009, MNRAS, 399, 683
Juszkiewicz R., Ferreira P. G., Feldman H. A., Jaffe A. H., Davis M., 2000, Sci, 287, 109
Kaiser N., 1987, MNRAS, 227, 1
Kaiser N., Efstathiou G., Saunders W., Ellis R., Frenk C., Lawrence A., Rowan-Robinson M., 1991, MNRAS, 252, 1
Kauffmann G., Nusser A., Steinmetz M., 1997, MNRAS, 286, 795
Larson D. et al., 2011, ApJS, 192, 16
Lavaux G., Tully R. B., Mohayaee R., Colombi S., 2010, ApJ, 709, 483
Linder E. V., 2005, Phys. Rev. D., 72, 043529
Lynden Bell D., Faber S. M., Burstein D., Davies R. L., Dressler A., Terlevich R. J., Wegner G., 1988, ApJ, 326, 19
Mandelbaum R., Seljak U., Kauffmann G., Hirata C. M., Brinkmann J., 2006, MNRAS, 368, 715
Masters K. L., Springob C. M., Haynes M. P., Giovanelli R., 2006, ApJ, 653, 861
Norberg P. et al., 2002, MNRAS, 332, 827
Nusser A., Branchini E., 2000, MNRAS, 313, 587
Nusser A., Davis M., 1994, ApJ, 421, L1
Nusser A., Davis M., 1995, MNRAS, 276, 1391
Nusser A., Davis M., 2011, MNRAS, submitted
Nusser A., Dekel A., 1993, ApJ, 405, 437
Nusser A., Dekel A., Bertschinger E., Blumenthal G. R., 1991, ApJ, 379, 6
Nusser A., da Costa L. N., Branchini E., Bernardi M., Alonso M. V., Wegner G., Willmer C. N. A., Pellegrini P. S., 2001, MNRAS, 320, L21
Peacock J. A., Smith R. E., 2000, MNRAS, 318, 1144
Peebles P. J. E., 1980, The Large-Scale Structure of the Universe. Princeton Univ. Press, Princeton
Pike R. W., Hudson M. J., 2005, ApJ, 635, 11
Press W. H., Teukolsky S. A., Vetterling W. T., Flannery B. P., 1992, Numerical Recipes in FORTRAN. The Art of Scientific Computing, 2nd edn. University Press, Cambridge
Radburn-Smith D. J., Lucey J. R., Hudson M. J., 2004, MNRAS, 355, 1378
Reid B. A., Percival W. J., Eisenstein D. J., Verde L., Spergel D. N., Skibba R. A., Bahcall N. A., 23+ SDSS Collaborators, 2010, MNRAS, 404, 60
Riess A. G., Davis M., Baker J., Kirshner R. P., 1997, ApJ, 488, L1
Schechter P. L., 1980, Astron. J., 85, 801
Sigad Y., Branchini E., Dekel A., 2000, ApJ, 540, 62
Skrutskie M. F. et al., 2006, AJ, 131, 1163
Springel V. et al., 2005, Nat, 435, 629
Springob C. M., Masters K. L., Haynes M. P., Giovanelli R., Marinoni C., 2007, ApJS, 172, 599
Springob C. M., Masters K. L., Haynes M. P., Giovanelli R., Marinoni C., 2009, VizieR Online Data Catalog, 217, 20599
Stark D. V., McGaugh S. S., Swaters R. A., 2009, ApJ, 138, 392
Strauss M. A., Willick J. A., 1995, Phys. Rep., 261, 271
Strauss M. A., Davis M., 1988, in Rubin V. C., Coyne G. V., eds, Large-Scale Motions in the Universe: A Vatican study Week. Princeton Univ. Press, NJ, p. 255
Tully R. B., Shaya E. J., Karachentsev I. D., Courtois H. M., Kocevski D. D., Rizzi L., Peel A., 2008, ApJ, 676, 184
Verde L. et al., 2002, MNRAS, 335, 432
Watkins R., Feldman H. A., Hudson M. J., 2009, MNRAS, 392, 743
Westover M., 2007, PhD thesis, Harvard University
Wild V. et al., 2005, MNRAS, 356, 247
Willick J. A., Courteau S., Faber S. M., Burstein D., Dekel A., Strauss M. A., 1997, ApJS, 109, 333
Yahil A., 1988, in Rubin V. C., Coyne G. V., eds, Large-Scale Motions in the Universe: A Vatican Study Week. Princeton Univ. Press, NJ, p. 219
Yahil A., Strauss M. A., Davis M., Huchra J. P., 1991, ApJ, 372, 380
Zaroubi S., 2002, preprint (astro-ph/0206052)
Zaroubi S., Branchini E., Hoffman Y., da Costa L. N., 2002, MNRAS, 336, 1234
Zehavi I. et al., 2010, ApJ, submitted (arXiv:1005.2413)

APPENDIX A: A NOTE ON ITERATIVE SCHEME

We caution of a possible systematic bias which may be important in iterative schemes for reconstructing velocities from the distribution of galaxies in redshift space. These schemes rely on the availability of a relation between the peculiar velocity and density in real space, e.g. the linear relation $f \operatorname{div} \boldsymbol{v} = -\delta$. At the end of any iteration intermediate peculiar velocities are provided, which are used as to derive the distances from the redshifts in the next iteration. Given those distances, the adopted real-space relation between δ and $\boldsymbol{v}$ is then solved to obtain a new guess for the velocities. The loop is continued until the change in the peculiar velocity between successive iterations becomes smaller than a certain threshold. Vanishing peculiar velocities could be taken as input for the first iteration.

We demonstrate here that the real-space distribution of galaxies as obtained from the output from any iteration scheme is biased. Hence, the corresponding peculiar velocity is also biased. We will first show that a biased distribution in real space is obtained even if unbiased but noisy peculiar velocities are used to get the distances. We write the density of galaxies in real space at distance r in a given direction on the sky as

$$n_{\rm e}(r)r^2 = (2\pi\sigma^2)^{-1/2} \int {\rm d}s s^2 n_{\rm s} {\rm e}^{-\frac{[s-v(s)-r]^2}{2\sigma^2}} \ , \tag{A1}$$

where $s = r + v$ is the radial redshift-space coordinate, $v(s)$ is the peculiar velocity of a galaxy present at s and σ is the rms of the error in the determination of the $v(s)$. In the above we assume normal error distribution and a one-to-one mapping between s and v, i.e. we neglect fingers-of-god effects and triple value zones. Working with the variable $r_1 = s - v(s)$ we get

$$n_{\rm e}(r)r^2 = (2\pi\sigma^2)^{-1/2} \int {\rm d}r_1 r_1^2 n_{\rm t}(r_1) {\rm e}^{-\frac{(r_1-r)^2}{2\sigma^2}} \ , \tag{A2}$$

where

$$n_t(r_1,) = \frac{{\rm d}s}{{\rm d}r_1} \left[1 + \frac{v(s(r_1))}{r_1}\right]^2 n_{\rm s}(s(r_1)) \tag{A3}$$

is the actual real-space density at r_1. Therefore, errors in the peculiar velocities (even if unbiased relative to the true ones) cause a smearing of structure in the radial direction. This anisotropic smearing is important for scales $\sim\sigma$ (in $\mathrm{km\,s^{-1}}$). The bias is similar to the traditional inhomogeneous Malmquist bias which is usually encountered in studies of distance indicators (Lynden-Bell et al. 1988).

Downloaded from https://academic.oup.com/mnras/article-abstract/413/4/2906/965330
by guest
on 27 February 2018

A self-consistent treatment of the bias should take into account the fact that $v(s)$ used in A2 and A3 is the biased peculiar velocity obtained from n_e. This could be done in the far observer limit, $|v/r| \ll 1$, and for small perturbations where equation (A3) reduces to

$$\delta_t = \delta_s + \frac{dv}{ds} \ . \tag{A4}$$

Substituting this into (A2) and Fourier transforming the result we get

$$\tilde{\delta}_e(\boldsymbol{k}) = [\tilde{\delta}_s(\boldsymbol{k}) + ik_r\tilde{v}(\boldsymbol{k})]\, e^{-k_r^2\sigma^2/2} \ , \tag{A5}$$

where k_r is the component of $\boldsymbol{k}$ parallel to the line of sight and the tilde denotes quantities in k-space. Using this last equation in the linear $\delta - v$ relation, $f\tilde{v} = -i(k_r/k^2)\tilde{\delta}_e$, we find

$$\tilde{\delta}_e(\boldsymbol{k}) = \frac{\tilde{\delta}_s(\boldsymbol{k})e^{-k_r^2\sigma^2/2}}{1 + f(k_r/k)^2 e^{-k_r^2\sigma^2/2}} \ , \tag{A6}$$

instead of the usual unbiased expression obtained with $\sigma = 0$.

A more complete analysis of the bias must incorporate the covariance of the errors in the derived peculiar velocity field.

This paper has been typeset from a TEX/LATEX file prepared by the author.

© 2011 The Authors, MNRAS **413,** 2906–2922
Monthly Notices of the Royal Astronomical Society © 2011 RAS

Downloaded from https://academic.oup.com/mnras/article-abstract/413/4/2906/965330
by guest
on 27 February 2018